

Alan M. Terpolilli

OVERALL HEAT TRANSFER COEFFICIENTS FOR
A HORIZONTAL CYLINDER IN A FLUIDIZED BED.

Thesis
T2764

The Pennsylvania State University
The Graduate School
Department of Mechanical Engineering

Overall Heat Transfer Coefficients
for a Horizontal Cylinder
in a Fluidized Bed

An Engineering Paper in
Mechanical Engineering

by

Alan M. Terpolilli

Submitted in Partial Fulfillment
of the Requirements for the
Degree of

Master of Science

April 1984

Approved By: Dr. James E. O'Brien
Title: Assistant Professor
Mechanical Engineering

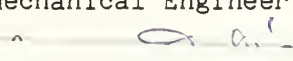


TABLE OF CONTENTS

ABSTRACT	i
INTRODUCTION	1
THE EXPERIMENTAL APPARATUS	3
General Arrangement	3
Fluidized Bed	4
Fluid Particles and Rotameters	5
Test Cylinder	6
Instrument Package	8
THE EXPERIMENTS	22
Procedure and Data Collection	22
Data Reduction	23
RESULTS AND DISCUSSION	31
Results	31
Discussion	37
CONCLUDING REMARKS	54
REFERENCES	56

LIST OF ENCLOSURES

Tables

1. Summary of particle name, bead sizes and meter used to measure flow
2. Results summary for particle size P-010
3. Results summary for particle size P-023
4. Results summary for particle size P-047
5. Results summary for particle size A-205
6. Results summary for particle size A-340
7. Particle name and corresponding data symbol
8. Summary of U_{opt} by particle size

Photographs

1. Fluidized bed apparatus
2. Close-up of fluidized bed containment vessel (test section)
3. Small rotameter
4. Large rotameter
5. Blue rotameter
6. Test cylinder assembled
7. Test cylinder separated to show heater cartridge
8. Instrument package

Figures

1. Schematic of overall flow and fluidized bed system

2. Detailed schematic of the fluidized bed
3. General design of the test cylinder
4. Outer surface of the test cylinder
5. Detailed design of the nylon end caps
6. Circuit diagram for the instrument package
7. Standardized data collection and reduction form
8. Large rotameter conversion curve of reading to SCFM
9. Heat transfer coefficient against relative mass velocity
10. Nusselt number based on particle diameter against relative mass velocity
11. Heat transfer coefficient against absolute mass velocity
12. Nusselt number based on outer wall tube diameter against absolute mass velocity
13. Comparison of experimental to empirical Nusselt numbers against absolute mass velocity for P-010
14. Comparison of experimental to empirical Nusselt numbers against absolute mass velocity for P-023
15. Comparison of experimental to empirical Nusselt numbers against absolute mass velocity for P-047
16. Comparison of experimental to empirical Nusselt numbers against absolute mass velocity for A-205
17. Comparison of experimental to empirical Nusselt numbers against absolute mass velocity for A-340

ABSTRACT

Total heat transfer coefficients were determined for a heated, copper cylinder placed horizontally in a fluidized bed. The fluidized particles were glass beads ranging in size from 215 μm to 3.40 mm. Fluidization was accomplished using air superficial velocities from 0.045 $\text{kg/m}^2\cdot\text{S}$ to 2.355 $\text{kg/m}^2\cdot\text{S}$. Temperatures were measured using thermocouples and the resulting h values tabulated and plotted as a function of superficial velocity and relative velocity. Nusselt numbers based on particle diameter and tube wall diameter were also determined. The results show consistent patterns with other workers and are substantiated by empirical correlations.

INTRODUCTION

Fluidized Bed Combustion is currently being studied intensely due to its very promising potential for producing clean and relatively inexpensive power from our nation's vast coal resources. Beds containing limestone or dolomite will absorb sulfur dioxide, thereby providing a sensible way to burn high-sulfur coals to generate power while maintaining high air quality standards without the use of expensive wet scrubbing equipment. Furthermore, the long-term goal of a pressurized fluidized-bed coal combustor which will generate steam and compressed hot gases to drive both steam and gas turbines in a combined power cycle holds the great promise of increasing the plant thermal efficiency by fully several percentage points over conventional power cycles.

Heat transfer between the combusting bed and the working fluid ordinarily takes place by means of submerged horizontal boiler tubes. Knowledge of the magnitudes of the heat transfer coefficients and temperature distributions along the tube surfaces is essential for an optimum design. The rate of heat transfer to a submerged tube depends upon a number of complex factors, including the properties of the bed material and the fluidizing gas, bed and tube geometries, and the fluidized state [1]. Many investigators have reported measurements of overall heat transfer between fluidized beds and horizontal tubes for a wide range of operating parameters [2-8].

Using a model of bed-to-surface heat transfer in which the total heat transfer consists of the additive contributions of gas convection and particle circulation, the heat transfer behavior may be determined.

Since particle circulation is difficult to measure, its contribution can be inferred from knowledge of the gas convective part and the total heat transfer coefficient. The gas convective component was measured by Matt Wade [9] in a separate set of experiments using a mass transfer analogy technique. The technique employs the use of a sublimating surface to indicate the convective component. The total heat transfer coefficients are determined in this paper and will be used for comparison to the gas convective results of [9].

Briefly, the investigation involves placement of a hollow, copper cylinder horizontally in a fluidized medium of glass beads. The cylinder represents a typical boiler tube and the glass beads are analogous to the boiler bed. Bed sizes were selected to model typical coal particle sizes. The cylinder has a heating cartridge placed in the hollowed portion which applies a uniform heat flux. Thermocouples are used to measure the bed temperature and resulting cylinder temperature. Knowing the heat applied and dimensions of the apparatus allow the total heat transfer coefficient to be calculated.

The results of these heat transfer experiments will be compared to the work of several previous investigators [2,4,7]. In addition, the present results will be utilized in determining the ratio of the gas convective component of heat transfer to the total heat transfer.

THE EXPERIMENTAL APPARATUS

General Arrangement

The experimental apparatus consists of a compressed air system, the containment bed, fluidized particles, the test cylinder and the instrumentation package. The air system produces, distributes, regulates, monitors and contains the working fluid. A general arrangement schematic is presented in Figure 1. Briefly, the figure depicts the oil-free compressor as the air source. This compressor delivers nearly 350 SCFM at 100 psia. This maximum flow rate was sufficient to provide fluidization over the entire range of particle sizes used in the experiments.

The distribution system is composed of 2 in. PVC pipe and fittings arranged in a convenient air-tight geometry. Pressure regulators, pressure gauges and overall flow meters were used to monitor and control the flow. The air then flows through one of two rotameters for flow rate measuring. The rotameter selection depends on the particle size and associated fluidizing velocity under study.

Flow control is achieved through the use of gate valves forward of the rotameter. The gate valve was selected instead of a globe valve to provide greater sensitivity in controlling the flow rate. After leaving the rotameter, the flow enters the diffuser where it is expanded to the dimensions of the bed itself. The pressure drop across the fluidized bed is observed by examining a mercury manometer tapped into the entrance of the diffuser. An air distributor system spreads the flow evenly to provide uniform fluidization. After

passing through the beads, the air is exhausted to the outside by means of galvanized duct work.

Fluidized Bed

Fluidization is accomplished in an 11-inch inside diameter plexiglass containment cylinder mounted vertically on supports. Figure 2 shows the bed in detail. The bed has a 6.5 inch x 9 inch removable access window with a matching leak-proof cover. The window allows the bed to be filled with particles as well as access to the test section.

The bead fill level is also indicated. This level is a constant regardless of the bead size under study. Two drain spouts allow the particles to be removed to independent levels. The upper level allows clearing only the test section while the lower spout is used to clear the entire containment of particles. The spouts are sealed with duct tape attached flush to the bed wall. This taping method minimizes flow disruption. The flow is left undisturbed by using smooth, polished inner walls and by having any protrusions away from the test section.

The base of the bed has a conical, 2 inch to 11 inch sheet metal diffuser acting to expand the compressed air. The length provides gradual, turbulent-free expansion. A distributor plate made up of a packed bed of 3.40 mm diameter glass beads sandwiched between two fine mesh brass screens forms the air distributor between the bed and the diffuser. The screens are 3 inches apart and secured by tack welds. The mesh of the screen is small enough to prevent the smallest

particle size, P-010 from falling through it into the air distribution system below.

The interface between the diffuser/upper screen and the bed is made by a gasket-filled flange connection. The gasket is a composite of 1/16 inch rubber material layers and tube type sealants. The flanged gasket seal maintains the air-tight integrity of the bed. The actual bed is shown in Photo 1. The advantage of using a plexiglas containment is apparent from the photograph. Namely, the extent of fluidization and general fluid behavior is clearly visible. Photo 2 also shows the bed when fluidized.

Fluid Particles and Rotameters

The fluidized particles are industrial quality glass spheres of various sizes. The glass is made inert from its lead-free, soda-lime silica composition. The spheres have uniform roundness and each size falls within a narrow band of dimensional variation. Since larger particles require successively greater volume flow rates to fluidize them, rotameters of different flow ranges must be used to maintain accuracy. Three meters were used having ranges of 1.35 SCFM to 27 SCFM, 12.82 SCFM to 160 SCFM and 100.5 SCFM to 1005 SCFM. They will be identified as small, large and blue, respectively. The first two occupy interchangeable positions and are shown in Photo 3 and Photo 4. The blue meter is identified by its color and is the monitoring meter in the distribution system. Photo 5 shows the blue meter. This meter is used because its range exceeds that of the large meter and because

meters of the same type as the large and small ones are not available in the appropriate size.

Table 1 summarized the bead identifier, average particle size and the meter used.

TABLE 1: Summary of Particle Name, Bead Sizes and Meter Used to Measure Flow

BEAD IDENTIFIER	AVERAGE SIZE (m)	METER
P-010	2.15×10^{-4}	Small
P-0230	5.125×10^{-4}	Large
P-0470	9.45×10^{-4}	Large Blue
A-205	2.03×10^{-3}	Blue
A-340	3.40×10^{-3}	Blue

The readings from the three meters were all converted to volume flow rates. In this way, the scale differences of the meters were eliminated and comparisons were made on a uniform basis. To better visualize the particle sizes, P-010 is about the size of table salt, P-0470 resembles large grain sand and A-340 is approximately the size of "BB's" for a pellet gun.

The Test Cylinder

A one-inch diameter copper cylinder is the focus of the experiment. Its seven inch length and 3/16 inch wall thickness were

designed to meet the heat transfer requirements of the experiment. Figure 3 and Figure 4 show the cylinder's design in detail. Copper was selected because of its high thermal conductivity, thus providing a uniform outer wall temperature when heated. To measure the temperature achieved and to verify the absence of circumferential differences, four chromel-alumel thermocouples were attached at 90° positions around the circumference. The thermocouple beads are attached below the wall surface and the wires run through machined grooves. The grooves are filled with thermal epoxy and sanded flush to the surface. In this manner, not only are the temperature characteristics unaltered but also the flow around the cylinder is left undisturbed.

An electrical heater cartridge is placed inside the cylinder's hollow core. The cartridge acts as a radially symmetric heat source to generate the desired temperature gradient between the test cylinder and the bed. The cartridge matches the cylinder in both length and diameter. To ensure effective conductive contact between the cartridge and the cylinder, thermally conductive paste was applied to the cartridge before inserting it into the cylinder. The combined effects of the planned tight fit and the paste minimized any possible contact resistance.

The cylinder is supported on two nylon end caps fastened into plexiglass clamps on the bed wall. Figure 5 shows the end caps or spacers. Paramount in their design is the matching with the copper cylinder of outer diameters, the fastening with recessed set screws, their length and the material selection. In this manner, the fluid flow is undisturbed and the test cylinder is positioned in the bed's

center. Heat transfer end effects may be ignored because of the extremely low thermal conductivity of the nylon material. As a further precaution, the thermocouple wires and cartridge power card run through a hollow spacer and exit the bed directly.

The assembled unit is shown in Photos 6 and 7. Photos 6 and 7 show the cylinder removed and partially disassembled for clarity.

Instrumentation Package

The instrument package is relatively simple. It consists of a variac power supply, a radial, multi-terminal switchbox, a digital voltmeter, chromel-alumel thermocouples and an insulated icebath. The circuit diagram depicting the component relationships is shown in Figure 6. The actual equipment used is presented on Photo 8.

The theory of operation combines the instruments to extract the temperature of the cylinder, the bed temperature and the power supplied. Other meaningful values may then be refined from the data. Briefly, the variac provides an adjustable current source to the heater cartridge. This source is indirectly measured by using the voltmeter. The voltage coupled with calibration information about the cartridge's resistance produces the power supplied to warm the cylinder. The digital voltmeter is a convenient and accurate measuring device for both AC and DC voltages present in the experiment. The DC potential differences arise from the use of thermocouples. The thermocouples use .010 m chromium wire and .010 m aluminum wire with teflon insulation. The thermocouples were manufactured in an inert gas environment by electric arc fusing. Manufacture using this

technique assures measured values corresponding closely to standardized Type K temperature conversion tables.

The radial switchbox is at the heart of the instrument package. It provides a common junction for all the thermocouples as well as providing easy selection of voltmeter inputs. Insulation packed in the switchbox minimizes false DC readings due to ambient temperature fluctuations. An insulated icebath is used as a reference for thermocouple voltage to temperature conversion. Careful use of distilled water and ice provided uniform reference from one data run to another. In addition to the cylinder and icebath thermocouples, three thermocouples indicate the inside bed temperatures. The thermocouples penetrate the bed wall at positions of $1/3$ the bed circumference and $1/3$ the elevation to the test section. This helical placement pattern averages out local temperature gradients to yield a good overall impression of bed temperature.

Data collection using the instruments discussed requires manual recording of voltmeter readings. Automated "Dataloggers" on the other hand, electronically scan, average and convert the readings to temperature. Attempts were made using a Monitor Labs 9302 datalogger but the results proved unsuccessful. The reason for the failure is attributed to excessive static discharge. The static is generated from the plexiglass bed's natural interaction with the glass beads. The charge then travels down the thermocouple wires into the datalogger causing problems ranging in severity from erroneous readings to complete microprocessor failure. Mitigating efforts included: grounding the bed, grounding the datalogger, installing terminal connection slunts, electrically insulating the test cylinder

with 4 coats of polyurethane and even applying commercial static minimizer sprays. Failure of all attempts to reduce the static to within the datalogger's acceptable limits forced the abandonment of automated data collection. The digital voltmeter proved to be less sensitive to the static and was selected as the logical alternative.

FIGURE 1: Schematic of Overall Flow and Fluidized Bed System

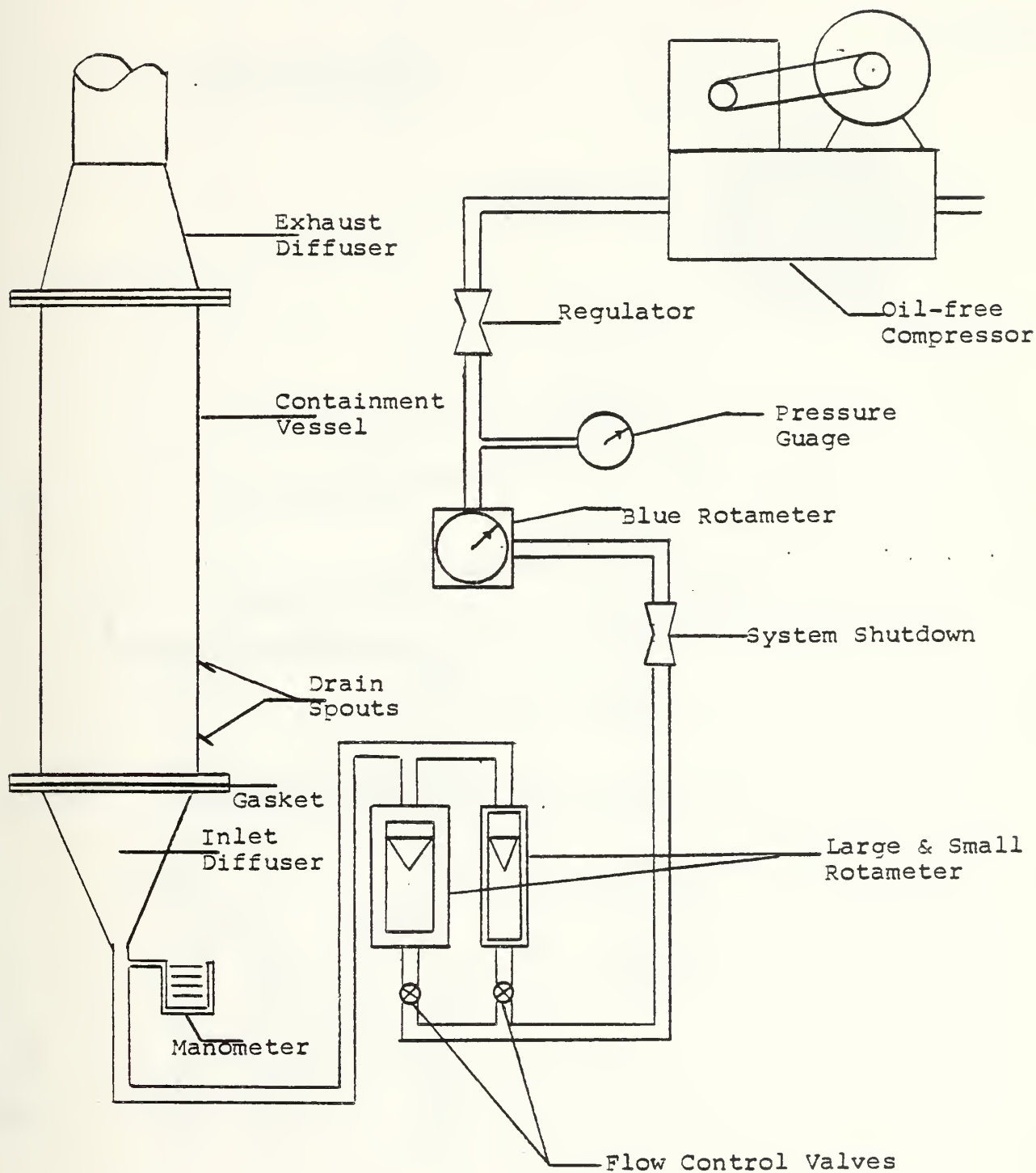
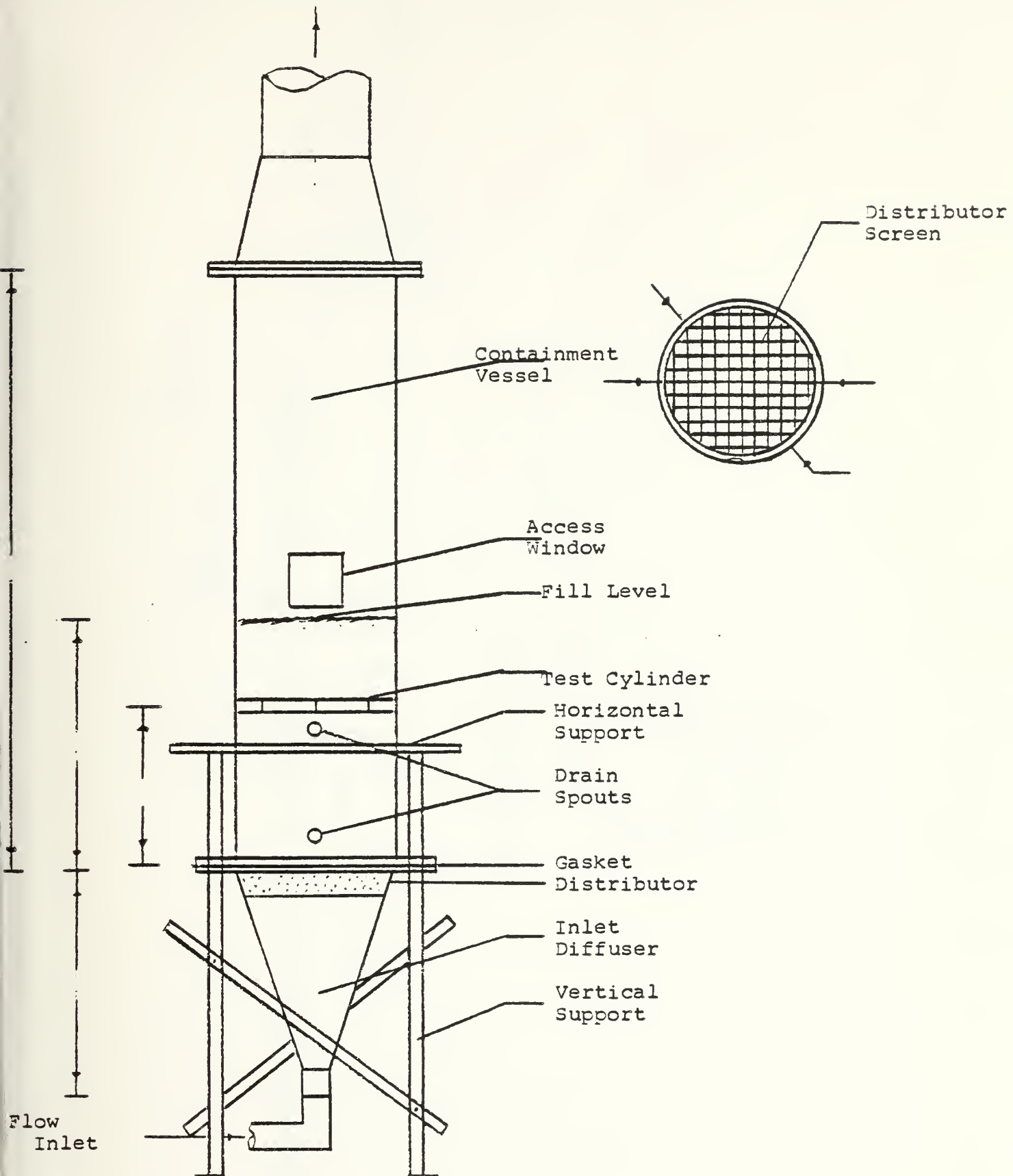
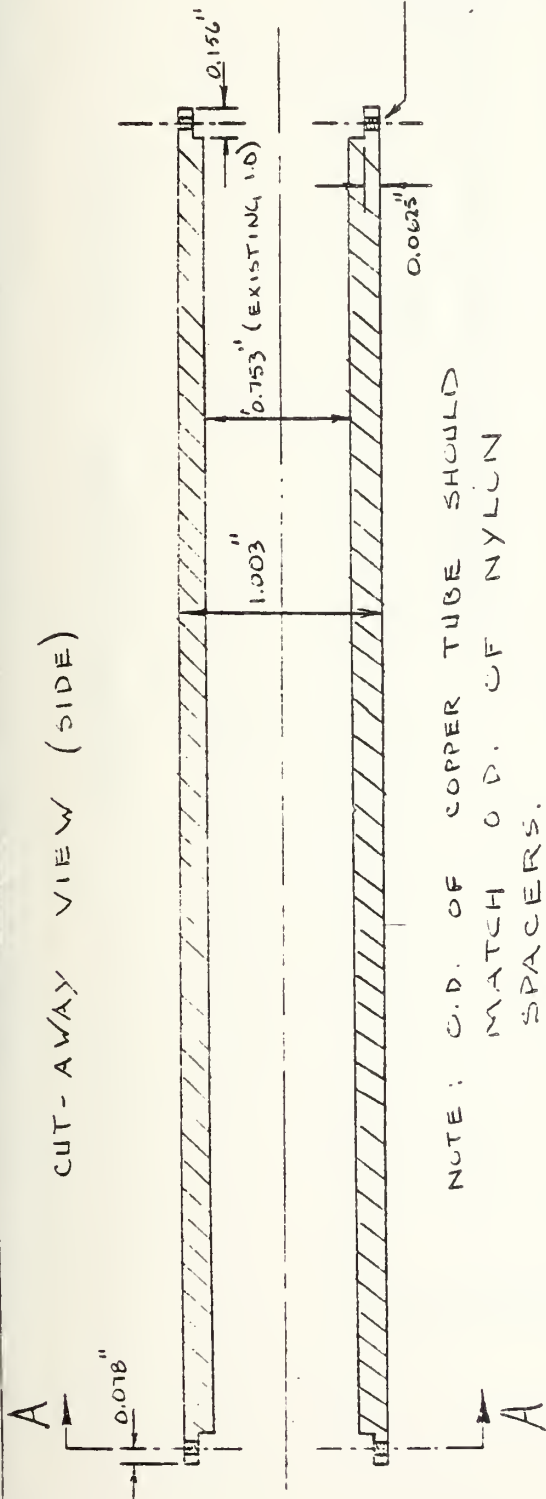
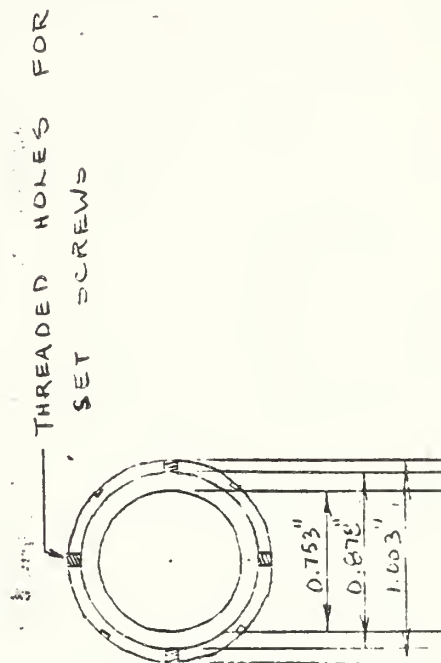


FIGURE 2: Detailed Schematic of the Fluidized Bed 12





SECTION A-A



THERMOCOUPLE GROOVES



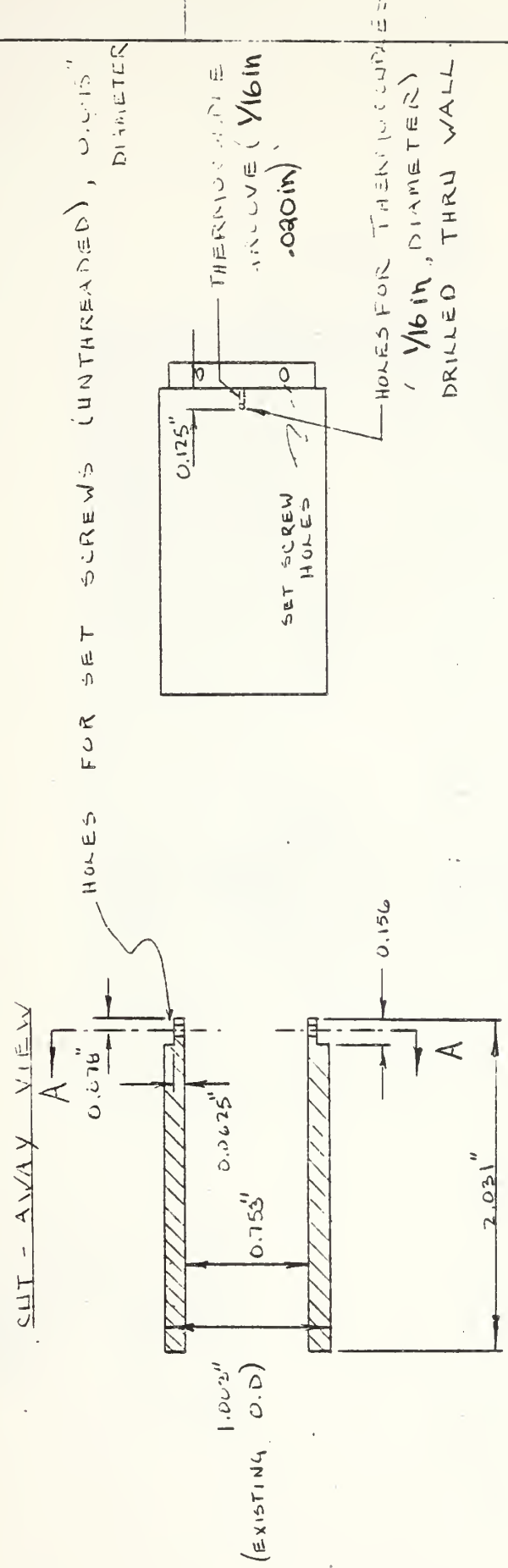
GROOVE DIMENSIONS:

WIDTH: $\frac{1}{16}$ in

DEPTH: .020 in

NOTE: GROOVES SHOULD BE LOCATED 90° APART
MIDWAY BETWEEN THE SET SCREWS
THERE WILL BE FOUR SUCH GROOVES.

FIGURE 5: Detailed Design of the Nylon End Caps



SECTION A - A

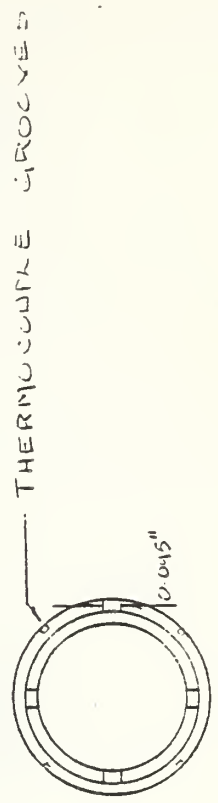
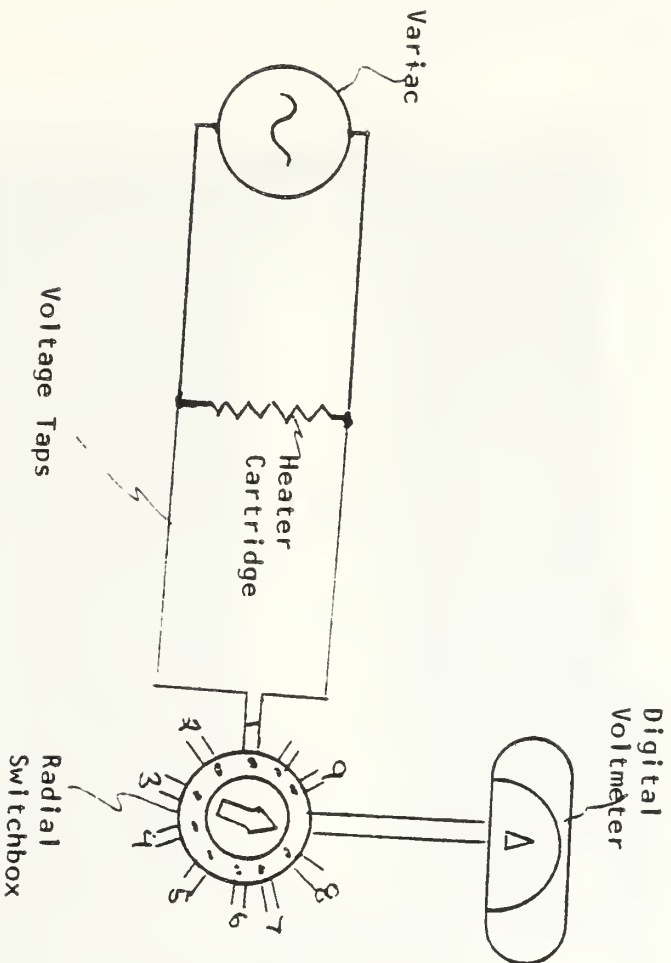


FIGURE 6: Circuit Diagram for the Instrument Package



Note: All Outputs Go to the Digital Voltmeter

Switchbox Inputs

1. Voltage Tap
2. Icebath
3. Bed
4. Bed
5. Bed
6. Cylinder
7. Cylinder
8. Cylinder
9. Cylinder

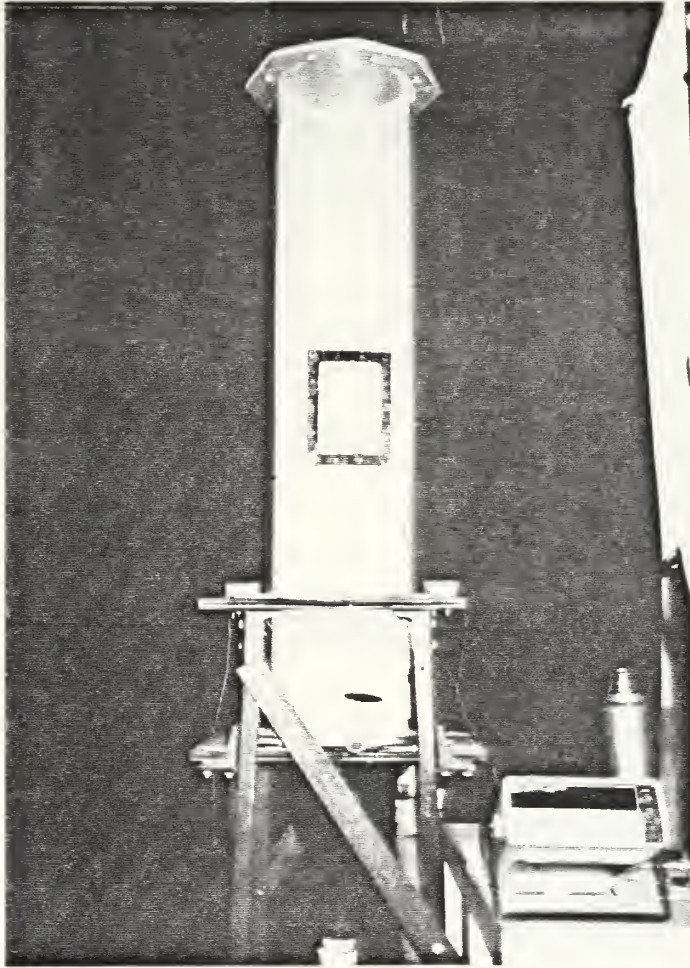


PHOTO 1: Fluidized Bed Apparatus

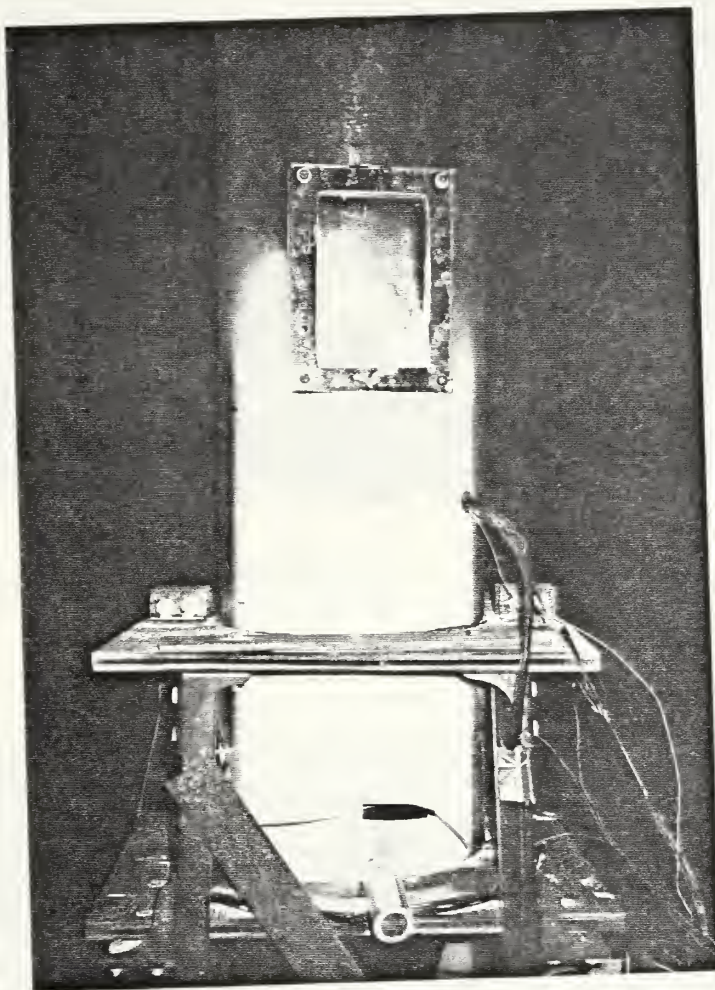


PHOTO 2: Close-up of Fluidized Bed Containment Vessel (Test Section)

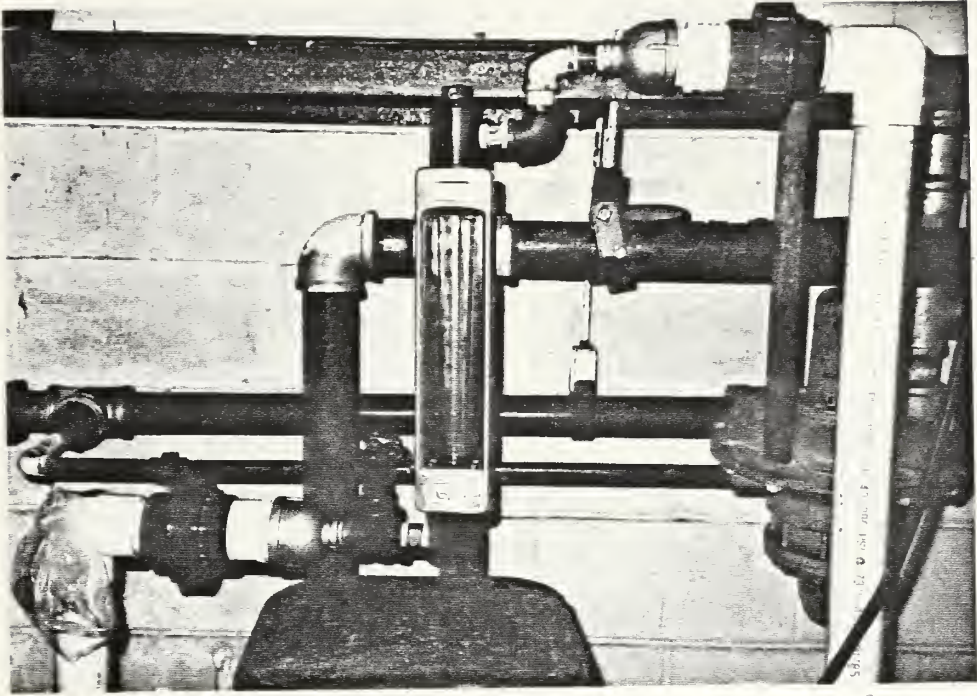


PHOTO 3: Small Rotameter

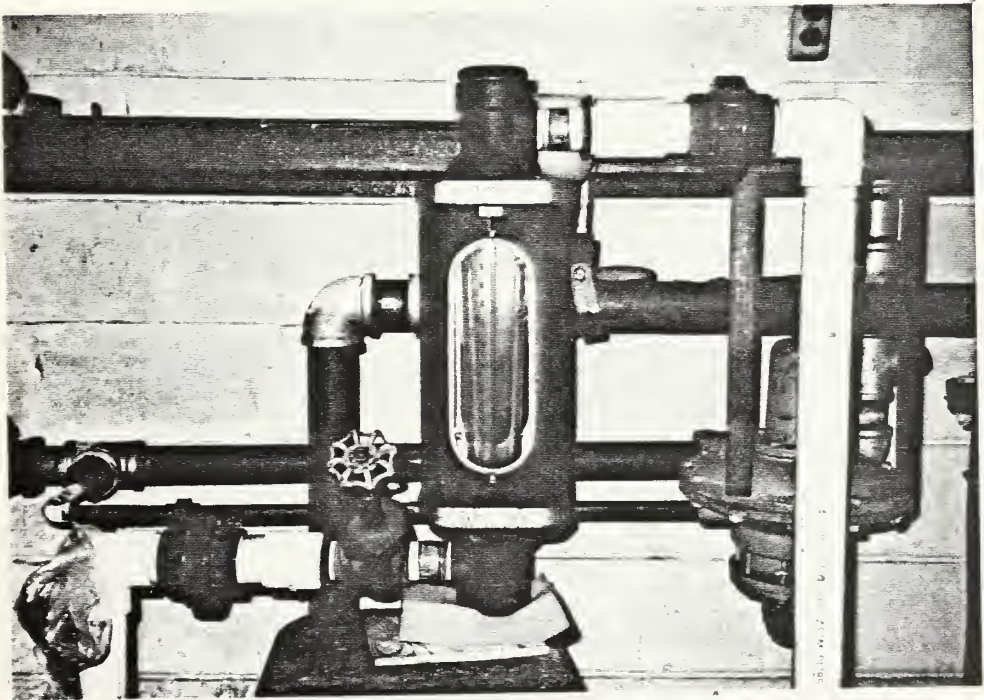


PHOTO 4: Large Rotameter

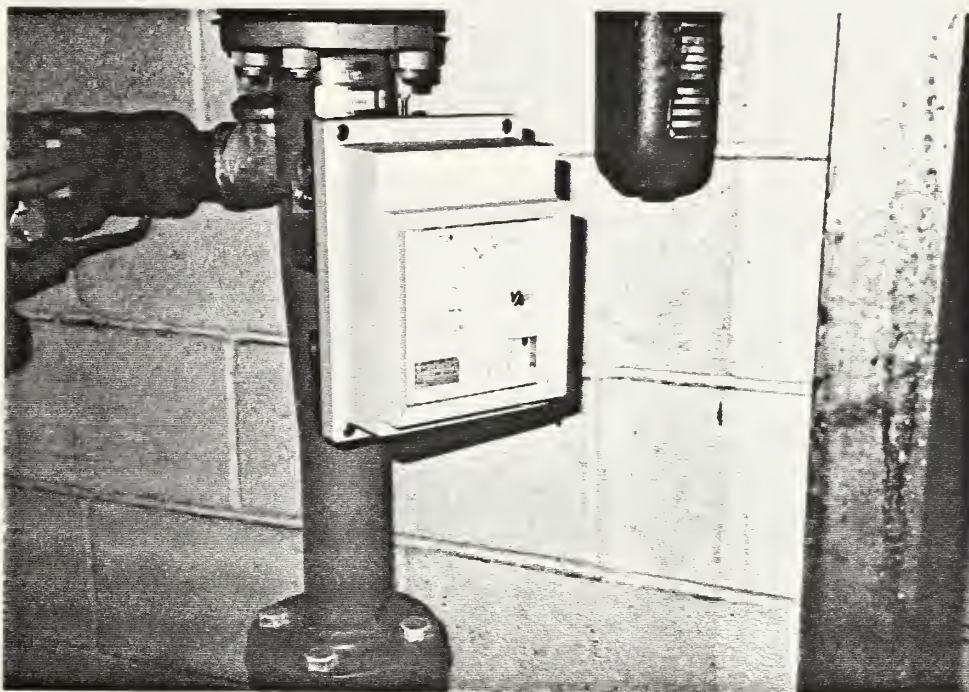


PHOTO 5: Blue Rotameter

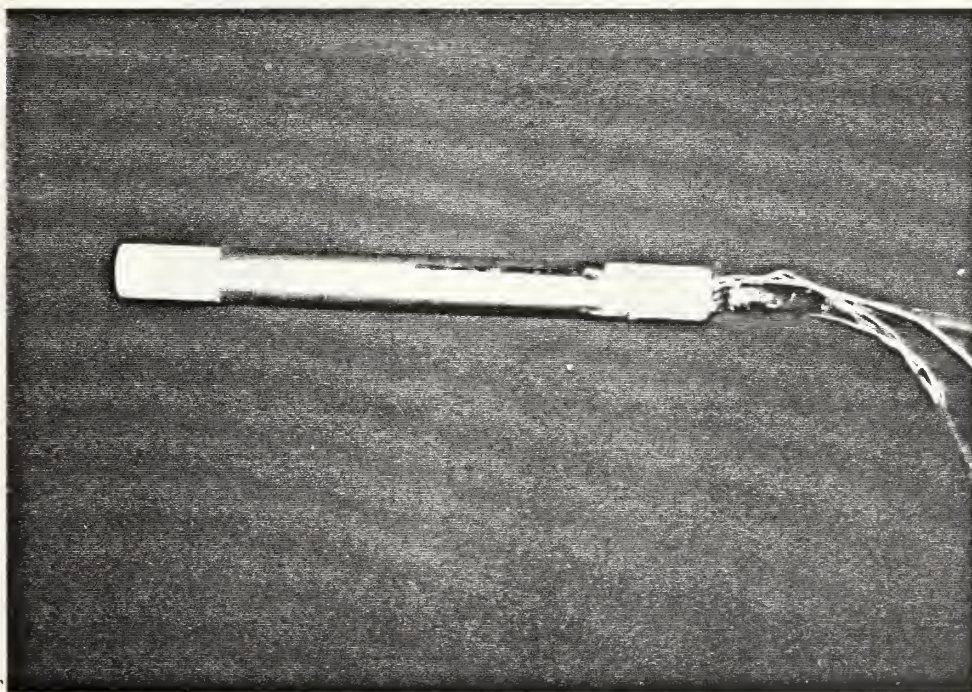


PHOTO 6: Test Cylinder Assembled

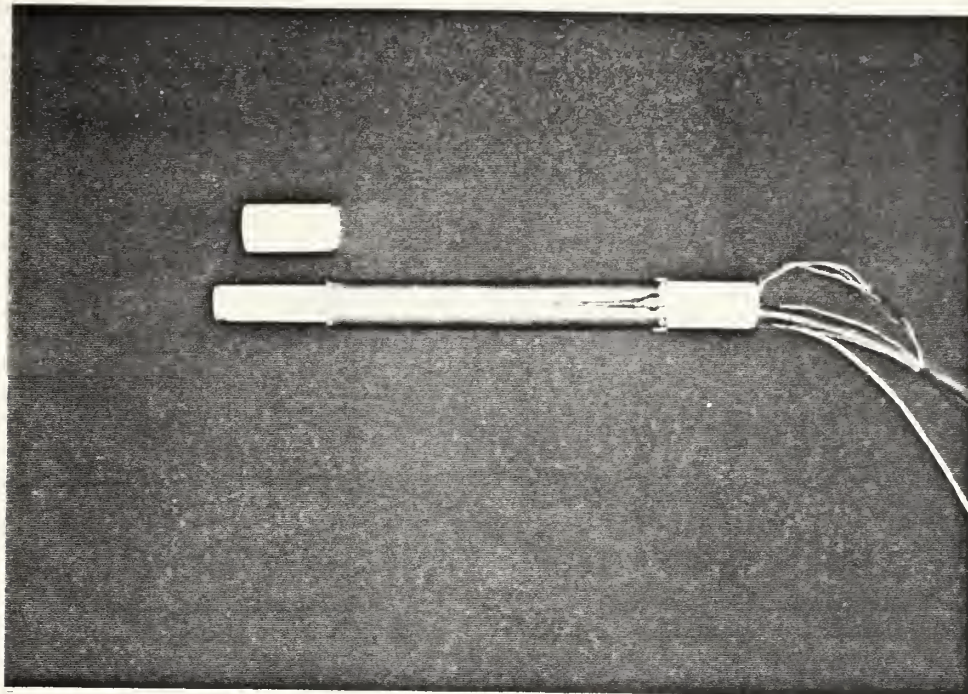


PHOTO 7: Test Cylinder Separated To Show Heater Cartridge

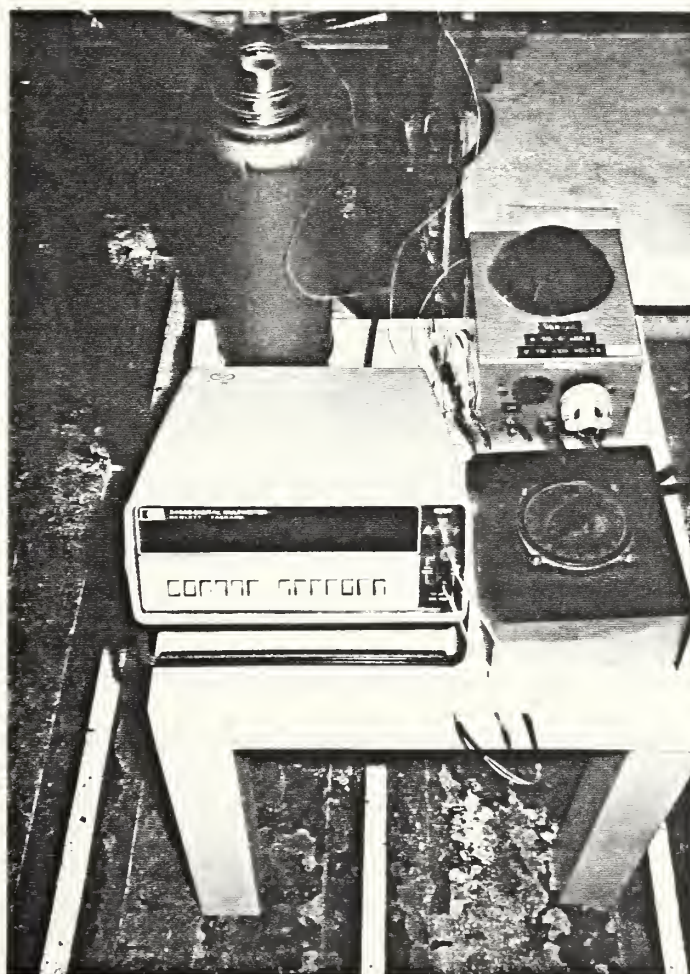


PHOTO 8: Instrument Package

THE EXPERIMENTS

Procedure and Data Collection

In an effort to minimize human errors an established experimental procedure was used. The standardized sequence steps were:

1. Start compressor and wait until operating pressure of 100 psi was obtained (15 min.)
 - 1a. Prepare icebath
2. Adjust air flow rate to achieve desired fluidization
3. Adjust variac to supply amperage where a temperature difference of about 10°C could be achieved
4. Wait until a steady-state temperature is achieved (10 min.)
 - 4a. Check steps 2 and 3
5. Collect data
6. Repeat steps 2-5

Data collection was also performed using a repeated series of events. To facilitate data collection and subsequent data reduction, a form depicting needed information was used. The form is presented in Figure 7. The form indicates locations to record voltage readings for the cylinder, bed, icebath and heater cartridge. The dial number is the corresponding terminal station on the radial switchbox. It is important to note the physical separation of the terminal stations. Separation prevents confusion and eliminates the possibility of erroneously recording data. The heater cartridge requiring AC volts to be read is separated from the thermocouples which require DC volts. The thermocouples are separated further into groups pertaining to what

temperature they are indicating. A reading is taken by selecting the dial number with appropriate voltage mode and observing the voltage displayed. This value is then recorded on the form. Fluctuations frequently occur because of the violent actions of the fluidized beads. When fluctuations occur, the changing values are observed and mentally averaged in an effort to isolate the true value. Errors of mental averaging are minimized by repeating the readings for five trials.

Data Reduction

For a given particle size at each flow rate, a separate data form was prepared. Examining Figure 7 reveals locations to reduce the data into meaningful information governing the heated cylinder's behavior in the fluid. Reduction begins in the upper section by numerically averaging the readings at a given dial number for all five trials. The subsequent results are then averaged for the cylinder and bed, respectively. Using the icebath as a reference, the final bed and cylinder voltage values are calculated. This calculated value is then converted to a temperature by using the NBS Type K conversion table and linear interpolation. The temperature gradient is found by finding the difference between the cylinder and bed temperature.

The heat supplied to produce the temperature gradient is found using the electrical expression.

$$Q = \frac{V^2}{R} = \text{heat supplied}$$

where: V = measured cartridge voltage

R = known resistance (53.45 ohms)

Using the determined temperature gradient, heat supplied and knowing the surface area of the cylinder; the desired heat transfer coefficient may be calculated. The governing relation is:

$$h = \frac{Q/A}{\Delta T}$$

where: h = overall heat transfer coefficient

A = cylinder surface area (0.0142 m²)

ΔT = temperature gradient (as measured)

Q = heat supplied

Nondimensional information is obtained by further data reduction to produce the Nusselt number based on particle diameter.

The Nusselt number based on particle diameter is determined by:

$$NU_p \# = \frac{hd_p}{K}$$

where: $NU_p \#$ = Nusselt number based on particle diameter

h = overall heat transfer coefficient

d_p = particle diameter in m

K = thermal conductivity of copper

(2.63 x 10⁻² W/m·°C)

The lower section of Figure 7 lends itself to programmed calculation. The large volume of data virtually necessitates programming.

To eliminate scale differences of the Nusselt number produced by using the various particle diameters as the characteristic dimension, the Nusselt number based on the outer diameter of the tube was determined. In this manner, a true indication of the total heat transfer coefficient is revealed for each particle size examined. The constant dimension allows direct comparison of Nusselt numbers between data sets. The Nusselt number based on the tube wall diameter was calculated by multiplying the existing Nusselt number based on particle diameter by the ratio of the wall tube diameter to the particle diameter. The governing relation is:

$$NU_{wt} = NU_p \left(\frac{D_T}{d_p} \right)$$

where: NU_{wt} = Nusselt number based on tube
diameter

NU_p = Nusselt number based on particle
diameter for each reading

D_T = outer wall diameter of the tube
(0.0254 m)

d_p = individual particle diameter in
meters

Air flow rates were standardized by determining the mass flow rate per minute through the fluidized area. This flow rate, called "G" is in units $kg/m^2 \cdot S$. Flow readings from the three meters were converted to the appropriate units using procedures particular to the meter used to measure the flow.

All conversion processes involve knowing the crosssectional area of the containment vessel. The area is determined by using the well known relationship for a circle. Based on a diameter of 11 inches and converting the result to m², the area is 0.063 m². This value becomes a constant for all calculations to determine "G".

The flow rate for all readings taken on the Small Meter is determined with the following relationship:

$$G = \frac{\%C\rho M}{A}$$

where: % = the decimal equivalent of flow read directly off the meter

C = capacity of the meter (27 ft³/min.)

ρ = air density at atmospheric pressure and room temperature (1.201 kg/m³)

A = crosssectional area of the containment vessel (0.0254 m)

M = metric conversion factor of ft³/min to m³/s (0.5886)

The process governing standardizing readings from the Large Meter is a two-step method. The first step involves using a prepared conversion curve which permits the rapid conversion of the meter's units into SCFM. Briefly, the curve is a plot of percent of flow read off the meter versus SCFM. The conversion curve is presented in Figure 8. The figure is used by entering with the % of flow read from the meter during experimentation on the x axis and recording the corresponding flow velocity in SCFM off the y axis. This value is then used in the

second step which is a direct calculation. The calculation is performed using the relation:

$$G = \frac{K\rho M}{A}$$

where: K = value determined from Figure 8 in
SCFM

ρ = air density at atmospheric pressure
and room temperature (1.201 kg/m³)

A = crosssectional area of the containment
vessel (0.0254 m)

M = metric conversion factor of ft³/min
to m³/S (0.5886)

Flow rate determination for the Blue Meter is a simple calculation involving:

$$G = \frac{\%C\rho M}{A}$$

where: % = decimal equivalent of flow read
directly off the meter

C = capacity of the meter (1005 ft³/min)

ρ = air density at atmospheric pressure
and room temperature (1.201 kg/m³)

A = crosssectional area of the containment
vessel (0.0254 m)

M = metric conversion factor of ft³/min
to m³/S (0.5886)

Using the above procedures results in flow measurements having the uniform dimensions of $\text{kg/m}^2 \cdot \text{s}$.

The ratio G/G_{\min} forms the dimensionless quantity which is used to indicate the relative magnitude of the flow rates used. The G_{\min} value is the smallest flow rate observed to fluidize the specific particle being studied. It then becomes the reference point from which to measure all other flow rates for that particle. Therefore, a G/G_{\min} ratio of 3 indicates the flow rate being used is three times the flow rate at the onset of fluidization.

Particle Size:

Flow Rate:

Location	Dial #	1 mV	2 mV	3 mV	4 mV	5 mV	1-5 Avg	↓ Avg
Cylinder	4							
	3							
	2							
	1							

Eed	U	18						
	m	17						
	L	16						

Ice bath	15	X	X	X	X	X	X	X	mV
----------	----	---	---	---	---	---	---	---	----

Htr. Cart.	11	X	X	X	X	X	X	X	V
------------	----	---	---	---	---	---	---	---	---

$$T_c = \text{---} \quad | \quad = \quad \text{mV} \Rightarrow \text{---}^{\circ}\text{C}$$

$$T_B = \text{---} \quad | \quad = \quad \text{mV} \Rightarrow \text{---}^{\circ}\text{C}$$

$$\Delta T = T_c - T_B = \text{---}^{\circ}\text{C}$$

$$Q = \frac{V^2}{R} = \frac{(\text{---})^2 V^2}{53.45 \Omega} = \text{---} \text{ W}$$

$$h = \frac{Q/A}{\Delta T} = \text{---} \frac{\text{W}}{\text{m}^2 \cdot ^{\circ}\text{C}}$$

where: $A = .0142 \text{ m}^2$

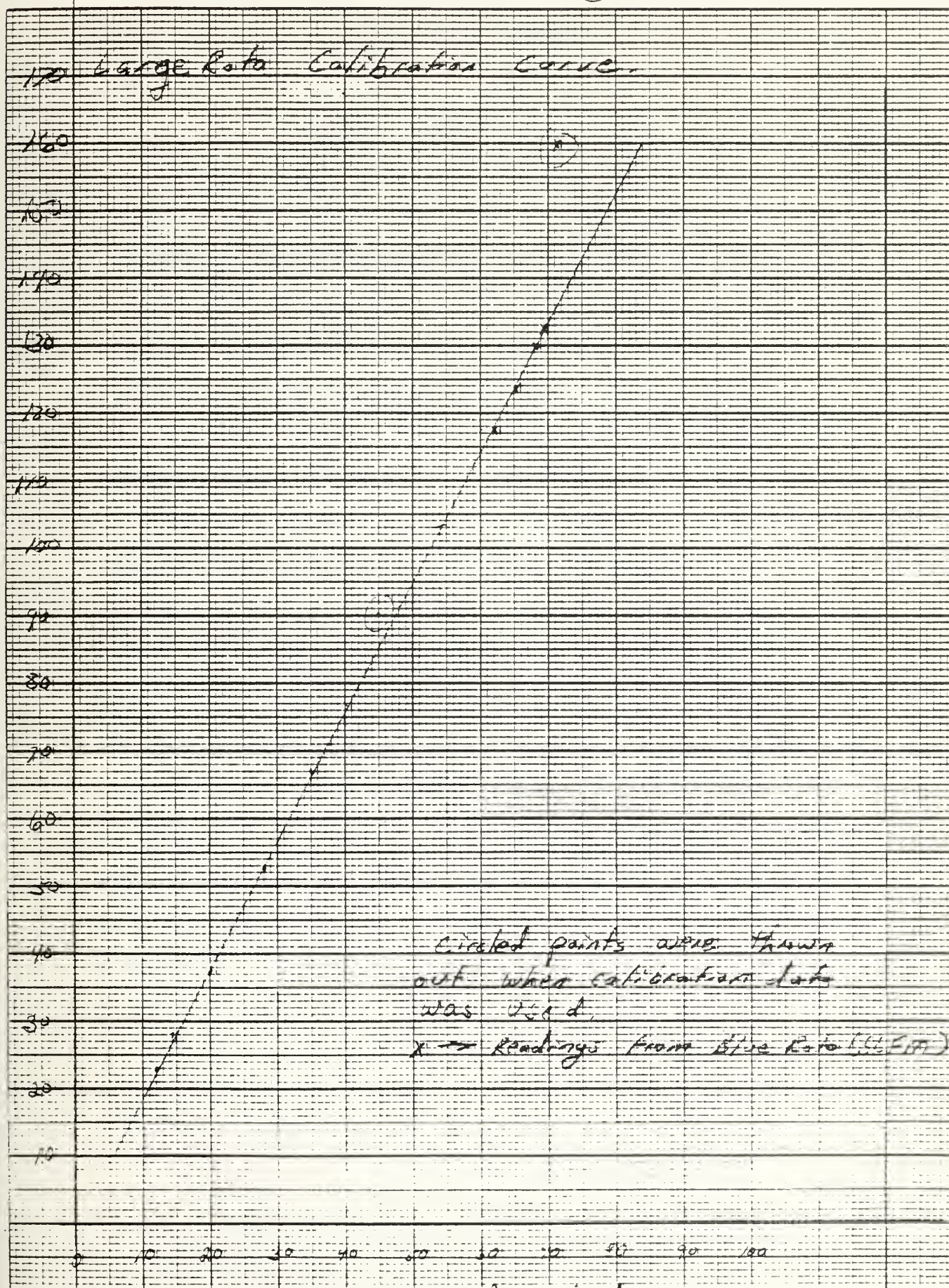
$$Nu \# = \frac{h d}{k} = \text{---}$$

$d = \text{particle diameter}$
 $k = 2.63 \times 10^{-2} \frac{\text{W}}{\text{m} \cdot ^{\circ}\text{C}}$

FIGURE 8: Large Rotameter Conversion of Reading to SCFM₃₀

WESTINGHOUSE ELECTRIC CORPORATION

(x) CURVE NO. _____



SIGNATURE _____

DATE _____

Roto Reading → CURVE NO. _____

RESULTS AND DISCUSSION

Results

Data was collected for each particle size at numerous flow rates. The assembled results relating the: air flow rate (G lbm/min·ft²), the ratio of a chosen flow rate to the minimum fluidizing flow rate (G/G_{\min}), the corresponding overall heat transfer coefficient (h W/m²·°C) and the dimensionless Nusselt number based on particle diameter (NU_p) and Nusselt number based on wall tube diameter (NU_{wt}) are presented by particle size. Tables 2-6 present the information for particle sizes P-010, P-0230, P-0470, A-205, A-340, respectively. Individual result summaries allow trends to be detected for each particle size. Relationships which link the results together are readily noticed from graphical representations. Figures 9, 10 and 11 plot results for all particle sizes together. Figure 9 presents the relationship of h to G/G_{\min} . Figure 10 presents NU_p as a function of G/G_{\min} . Figure 11 shows the relationship of h to G . Figures 13-16 plot NU_{wt} vs. G by individual particle sizes. Also indicated on each graph, are the predicted results obtained from published correlations. The Nusselt number based on tube wall diameter is graphically compiled on Figure 12.

TABLE 2: Results Summarized for Particle Size P-010

$$G_{\min} = 0.045 \text{ kg/m}^2 \cdot \text{s}$$

$$d = 2.15 \times 10^{-4} \text{ m}$$

$$k = 2.63 \times 10^{-3} \text{ W/m}^\circ\text{C}$$

G	G/G _{min}	h	NU _p	NU _{wt}
0.045	1.000	130.032	1.063	125.582
0.062	1.388	193.741	1.584	187.133
0.075	1.665	248.656	2.033	240.178
0.085	1.888	250.647	2.049	242.068
0.101	2.248	292.851	2.394	282.826
0.110	2.442	306.088	2.502	295.585
0.120	2.665	309.111	2.527	298.539
0.137	3.053	326.214	2.667	315.078
0.160	3.553	347.681	2.842	335.753
0.170	3.775	351.797	2.876	339.769
0.180	3.996	364.600	2.981	352.174
0.194	4.330	377.377	3.085	364.460
0.199	4.440	383.948	3.139	370.840
0.209	4.663	397.218	3.247	383.599
0.219	4.884	400.809	3.277	387.143

TABLE 3: Results Summary for Particle Size P-0230

$$\begin{aligned}
 G_{\min} &= 0.256 \text{ kg/m}^2 \cdot \text{s} \\
 d &= 5.125 \times 10^{-4} \text{ m} \\
 k &= 2.63 \times 10^{-2} \text{ W/m}^\circ\text{C}
 \end{aligned}$$

G	G/G _{min}	h	NU _p	NU _{wt}
0.256	1.000	79.680	1.553	76.968
0.315	1.228	168.347	3.281	162.610
0.351	1.370	219.596	4.279	212.071
0.402	1.570	266.210	5.188	257.122
0.449	1.750	272.246	5.305	262.921
0.469	1.829	273.322	5.326	263.962
0.474	1.848	277.788	5.413	268.274
0.517	1.992	280.041	5.457	270.454
0.530	2.068	279.373	5.444	269.810
0.564	2.202	282.021	5.496	272.387
0.609	2.378	275.595	5.370	266.142
0.693	2.702	273.368	5.327	264.011
0.785	3.063	275.730	5.373	266.291

TABLE 4: Results Summary for Particle Size P-047

$$\begin{aligned}
 G_{\min} &= 0.564 \text{ kg/m}^2 \cdot \text{s} \\
 d &= 9.45 \times 10^{-4} \text{ m} \\
 k &= 2.63 \times 10^{-2} \text{ W/m}^\circ\text{C}
 \end{aligned}$$

G	G/G _{min}	h	NU _p	NU _{wt}
0.564	1.000	136.711	4.912	132.026
0.694	1.204	217.665	7.821	210.215
0.774	1.344	233.424	8.387	225.428
0.827	1.435	236.467	8.497	228.385
0.949	1.647	221.256	7.950	213.683
1.009	1.750	223.253	8.022	215.618
1.061	1.841	216.326	7.773	208.925
1.108	1.923	214.844	7.720	207.501
1.126	1.953	220.619	7.927	213.064
1.154	2.003	216.220	7.769	208.818
1.175	2.039	218.988	7.869	211.505
1.201	2.083	215.056	7.727	207.689
1.243	2.156	217.666	7.821	210.216
1.302	2.259	213.805	7.682	206.479
1.478	2.563	209.431	7.525	202.259
1.709	2.965	206.457	7.418	199.383

TABLE 5: Results Summary for Particle Size A-205

$$\begin{aligned}
 G_{\min} &= 1.201 \text{ kg/m}^2 \cdot \text{s} \\
 d &= 2.03 \times 10^{-3} \text{ m} \\
 k &= 2.63 \times 10^{-2} \text{ W/m}^\circ\text{C}
 \end{aligned}$$

G	G/G _{min}	h	NU _p	NU _{wt}
1.201	1.000	151.826	11.719	146.632
1.311	1.092	177.623	13.710	171.544
1.478	1.195	196.474	15.165	189.750
1.598	1.330	192.909	14.890	186.308
1.662	1.384	195.224	15.053	188.348
1.755	1.461	187.899	14.503	175.836
1.847	1.538	185.272	14.300	178.926
1.939	1.615	181.972	14.046	175.748
2.032	1.692	181.494	14.009	175.285
2.124	1.769	175.123	13.517	169.128
2.216	1.846	170.357	13.149	164.524
2.309	1.922	170.367	13.150	164.537

TABLE 6: Results Summary for Particle Size A-340

$$\begin{aligned}
 G_{\min} &= 1.662 \text{ kg/m}^2 \cdot \text{s} \\
 d &= 3.40 \text{ mm} = 3.40 \times 10^{-3} \text{ m} \\
 k &= 2.63 \times 10^{-2} \text{ W/m}^\circ\text{C}
 \end{aligned}$$

G	G/G _{min}	h	NU _p	NU _{wt}
1.662	1.000	166.788	21.562	161.080
1.755	1.055	165.664	21.417	159.998
1.847	1.111	171.140	22.125	165.287
1.939	1.167	181.715	23.492	175.499
2.032	1.222	190.338	24.606	183.821
2.124	1.278	191.537	24.761	184.979
2.216	1.333	191.649	24.776	185.091
2.309	1.389	191.337	24.736	184.792
2.355	1.417	194.510	25.146	187.855

Discussion

Examination of the results supports the achievement of the experimental goal, that is, to identify the total heat transfer behavior for all particle sizes specific to the bed under study. Published values or correlations vary according to the physical make-up of the particular bed studied. Physical factors affecting the heat transfer properties include: size, type and weave of the distributor plate, the size, shape and thermal properties of the fluidized particles, moisture content of the air and lastly, the dimensions of the bed. The relationship between particle sizes and the trends of a given bead size are most readily noticed from graphical displays. Figure 11 shows the behavior of the total heat transfer coefficient as the absolute flow increases for all bead sizes. Figure 10 depicts the characteristic Nusselt number based on particle diameter for flow rates above minimum fluidization. Figure 9 shows h as a function of relative flow. All particle sizes are plotted together. To identify the individual particle sizes, different data symbols are used. The symbols are presented in Table 7 and on each graph for clarity.

Examining the plot of h vs. G/G_{\min} or Figure 9 produces interesting observations. The smallest particle sizes tend to have the highest total heat transfer coefficient. This behavior is most evident at G/G_{\min} values above 1.4. So, as particle size increases, total heat transfer decreases, in agreement with many previous investigations [2,4,7]. The decrease of total heat transfer with particle size is due to the increasing importance of gas convection

for the larger particle sizes. By tracing each particle size individually, a repeated pattern is noticed. The pattern tends to be one of rapid increase of h for a reasonably small change in G/G_{\min} until a maximum h is achieved at a specific G/G_{\min} . After this unique point, the h value decreases slowly for higher flow rates. Particles P-047 and A-205 demonstrate the behavior most dramatically. Bead size P-010 was not observed in a flow rate range large enough to include its maximum.

TABLE 7: Particle Name and Corresponding Data Symbol

SYMBOL	BEAD IDENTIFIER
▽	P-010
○	P-023
□	P-047
⬡	A-205
△	A-340

The uniqueness of a particular flow rate corresponding to a maximum h value is clearly seen in Figure 11. On this figure, the G at the largest total heat transfer coefficient may be read directly from the graph. The value of fluidizing velocity at which the maximum in h occurs is called the optimum velocity, U_{opt} . It has been observed by many investigators [10] and a correlation provided by Toades [11] may be used to predict its value. The correlation presents the optimum Reynolds number. The correlation yields the corresponding U_{opt} value to within a multiplied constant involving the

specific kinematic fluid viscosity and the characteristic length of the apparatus used. The expression becomes:

$$U_{opt} = \frac{Ar}{18 + (5)(22\sqrt{Ar})} \left(\frac{Y}{L}\right)$$

where: Ar = the Archimeder number

Y = kinematic viscosity of air

(1.55 x 10⁵ m²/s)

L = characteristic length or the diameter
of each particle size

This relationship was applied for all particle sizes and the results compared to the experimental results of the present study. Table 8 compiles the information by particle size.

TABLE 8: Summary of U_{opt} by Particle Size

U_{opt} (m/s)

Beads	Experiment	Correlation
P-010	Not Applicable	0.3580
P-023	0.4225	0.5972
P-047	0.6886	0.8379
A-205	1.2306	1.2293
A-340	1.6919	1.5941

The correlation velocities fit the experimental results very well for the largest two particle sizes, however the agreement is not quite as

good for the intermediate particle sizes. Total heat transfer decreases at velocities above the optimum velocity because of the increasing importance of gas convection heat transfer. As the fluidizing velocity is increased, a corresponding increase in bed porosity occurs. The excess fluid separates the particles which diminishes the strong contribution of particle heat conduction, thereby lessening the overall heat transfer.

Closer examination of the h vs. G plot shown in Figure 11 indicates that the dependency of h on G is stronger for smaller particle sizes. That is, the slope of the curve is greater for small beads. Using Figure 9, the steep rise is obvious when beads P-023 and P-047 are compared to A-205 and A-340. For G/G_{\min} values from 1.0 to about 1.6, the h values of the smaller particles changed from about 80 to 265 and 135 to 236, respectively as compared to 150 to 195 and 165 to 190, respectively for the larger particles.

This behavior may be explained by considering the mechanisms involved which compare the overall heat transfer coefficient. It is the sum of a conductive part and gas convective part. For smaller particles, the h value is dominated by particle conduction. Heat transfer predominantly caused the physical touching of packets of particles to the heated cylinder. Whereas for the largest particles, the overpowering mechanism is gas convection.

Figure 10 plots the Nusselt number based on particle diameter versus relative flow rate for all particles. The plot clearly indicates that each bead size has a characteristic range of Nusselt number. The band tends to be narrow and at successively higher values as bead size increases. The increase in Nusselt number with

increasing particle size does not indicate conflicting results as presented in Figure 11. The Nusselt number calculation is controlled by the particle diameter dimension. This dimension overpowers the h value. The general shape of the curves for both figures is consistent with the earlier work of others [2,4,7].

Nusselt numbers based on particle diameters can be somewhat misleading. They may erroneously imply that heat transfer increases with increasing bead size. Nusselt numbers based on the tube wall diameter accurately portray the physical occurrence since the tube wall diameter is constant. Compare the implied behavior of Figure 12 for NU_{wt} as a function of G using all particle sizes to that of Figure 10. As expected, the plotted curves have shapes identical to the plots of h on G . Figure 12 shows that the total heat transfer coefficient increases with decreasing bead size.

Detailed examination of NU_{wt} in relation to G for individual particles is presented in Figures 13-17. Each display also has the behavior predicted by the three most applicable correlations. The correlations proposed by Grewal and Saxena [7], Andeen and Glicksman [4], and Vreendenberg [2] are shown below. Each investigator attempted to account for the many factors which affect heat transfer in a fluidized bed.

Grewal & Saxena:

$$NU_{wt} = 47(1 - \epsilon) \left(\frac{GD_T \rho_s}{\rho_f \mu} \frac{\mu^2}{d_p^3 \rho_s^2 g} \right)^{0.325} \left(\frac{\rho_s C_{ps} D_T^{3/2} g^{1/2}}{k_f} \right)^{0.23} Pr^{0.30}$$

where

$$\epsilon = \frac{1}{2.1} \left[0.4 + \left\{ 4 \left(\frac{\mu G}{d_p^2 (\rho_f (\rho_s - \rho_f) \phi_s g)} \right)^{0.43} \right\}^{1/3} \right]$$

Andeen & Glicksman:

$$NU_{wt} = 900(1 - \epsilon) \left[\left(\frac{GD_T \rho_s}{\rho_f \mu} \right) \left(\frac{\mu^2}{d_p^3 \rho_s^2 g} \right) \right]^{0.326} Pr^{0.3}$$

where:

$$\epsilon = \frac{1}{2.1} \left\{ 0.4 + \frac{200 G \mu}{d_p^2 \rho_f (\rho_s - \rho_f) g} \right\}^{1/3}$$

Vreendenberg:

$$NU_{wt} = 420 \left[\left(\frac{G D_T \rho_s}{\rho_f \mu} \right) \left(\frac{\mu^2}{d_p^3 \rho_s^2 g} \right) \right]^{0.3} Pr^{0.3}$$

The nomenclature common to all the correlations and the values which correspond to this experimental setup are as follows:

- ϵ = bulk porosity (as determined above)
- G = superficial mass fluidizing velocity (G in. $\text{kg/m}^2 \cdot \text{s}$)
- D_T = outside tube diameter (0.0254 m)
- ρ_s = density of the bed material - for glass beads (2500 Kg/m^3)
- ρ_f = density of the fluidizing air (1.201 kg/m^3)

- μ = fluidizing air viscosity ($184 \times 10^{-7} \text{ N}\cdot\text{s}/\text{m}^2$)
- d_p = particle diameter as shown on TABLE 1
- g = acceleration due to gravity ($9.81 \text{ m}/\text{s}^2$)
- C_{ps} = specific heat of the bed material - for glass beads ($750 \text{ J}/\text{kg}\cdot^\circ\text{K}$)
- K_f = thermal conductivity of the fluidizing air ($26.3 \times 10^{-3} \text{ W}/\text{m}\cdot^\circ\text{K}$)
- Pr = Prandtl number of air (0.707)
- ϕ_s = sphericity of the beads (assumed to be 1)

For the smallest particle size, P-010, the Andeen and Glicksman correlation most accurately represents the data. Figure 13 shows the experimental NU_{wt} values and the correlation values as a function of G . This representation is about 10% different from measured values. Figure 14 presents the same information for P-023. Here, the Grewal and Saxena correlation coupled with the Andeen and Glicksman correlation form the upper and lower bounds, respectively. Both correlations could be interpreted to represent the data. The Grewal and Saxena correlation is most accurate for intermediate superficial velocities. At larger flow rates, the Andeen and Glicksman model is most applicable. It should be noted that none of the correlations account for the rapid increase of the heat transfer coefficient at the smallest flow rates for either P-010 and P-023.

Figures 15, 16, 17 present the experimental and correlated behavior for bead sizes P-047, A-205, A-340, respectively. The experimental results are very poorly predicted by the three mathematical models in all cases. The correlations anticipate NU_{wt} values significantly lower than those actually achieved. The correlations were intended to be used for particles less than 500

micrometers. Since the last three bead sizes clearly exceed the particle size limit, extrapolation may not be valid. The results are qualitatively compatible and quantitatively substantiated by the work of others in the field.

FIGURE 9: Heat Transfer Coefficient Against Relative Mass Velocity

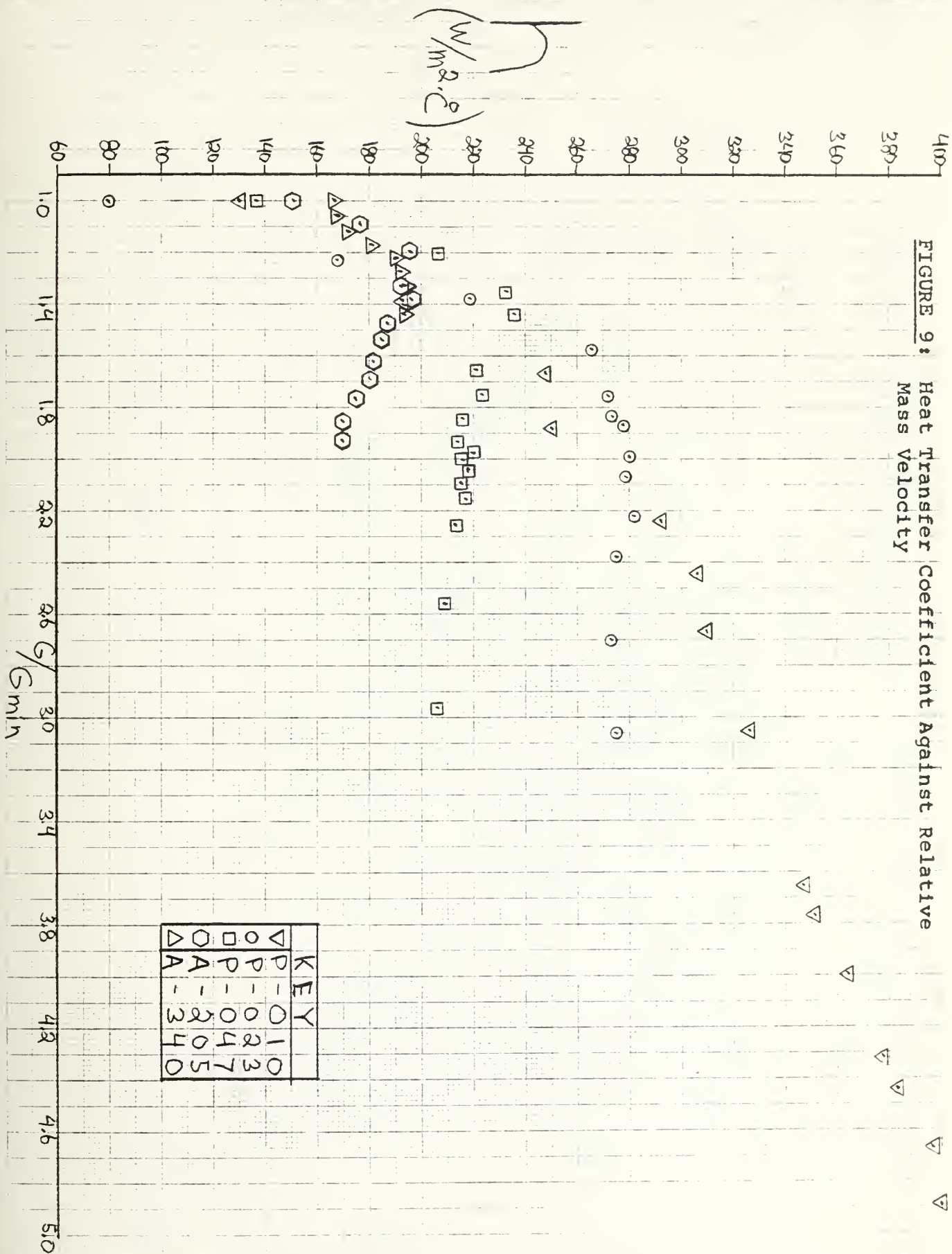
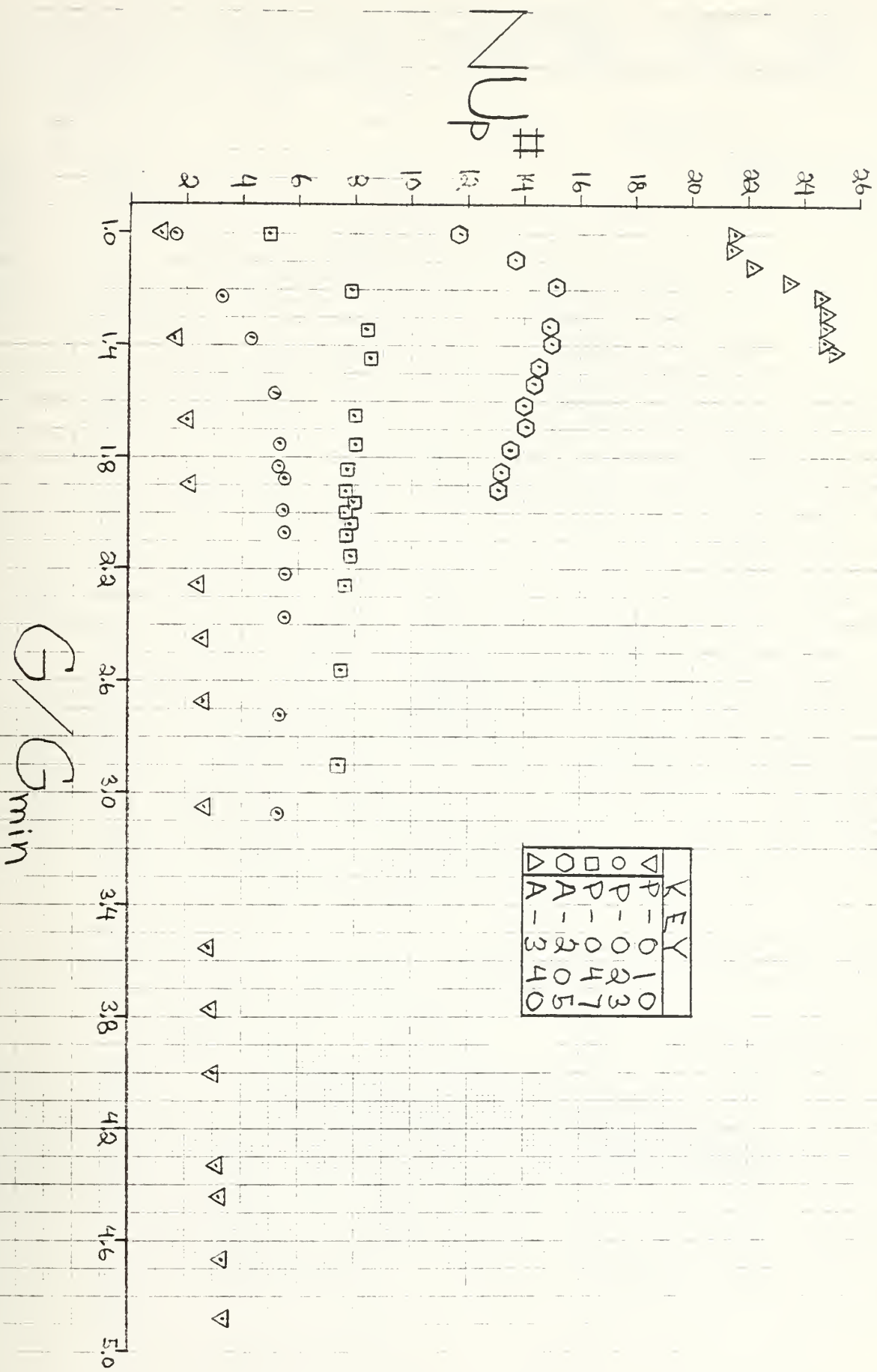
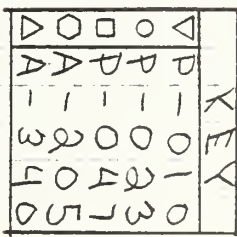


FIGURE 10: Nusselt Number Based on Particle Diameter Against Relative Mass Velocity





G (Kg/m²s)

3. (M/M/2)

FIGURE 12: Nusselt Number Based on Particle Diameter Against Absolute Mass Velocity

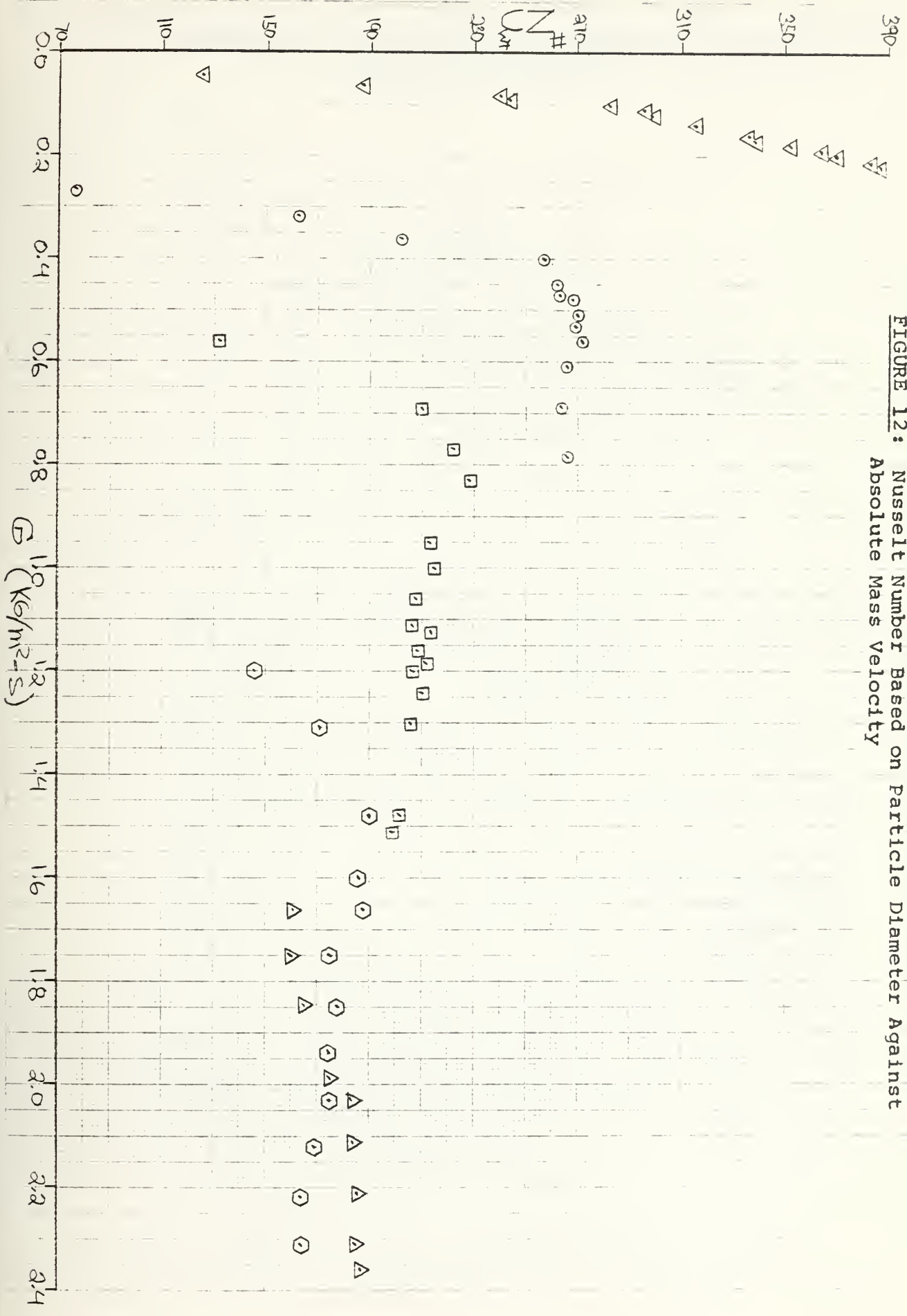


FIGURE 13: Comparison of Experimental to Empirical Nusselt Numbers Against Absolute Mass Velocity for P-010

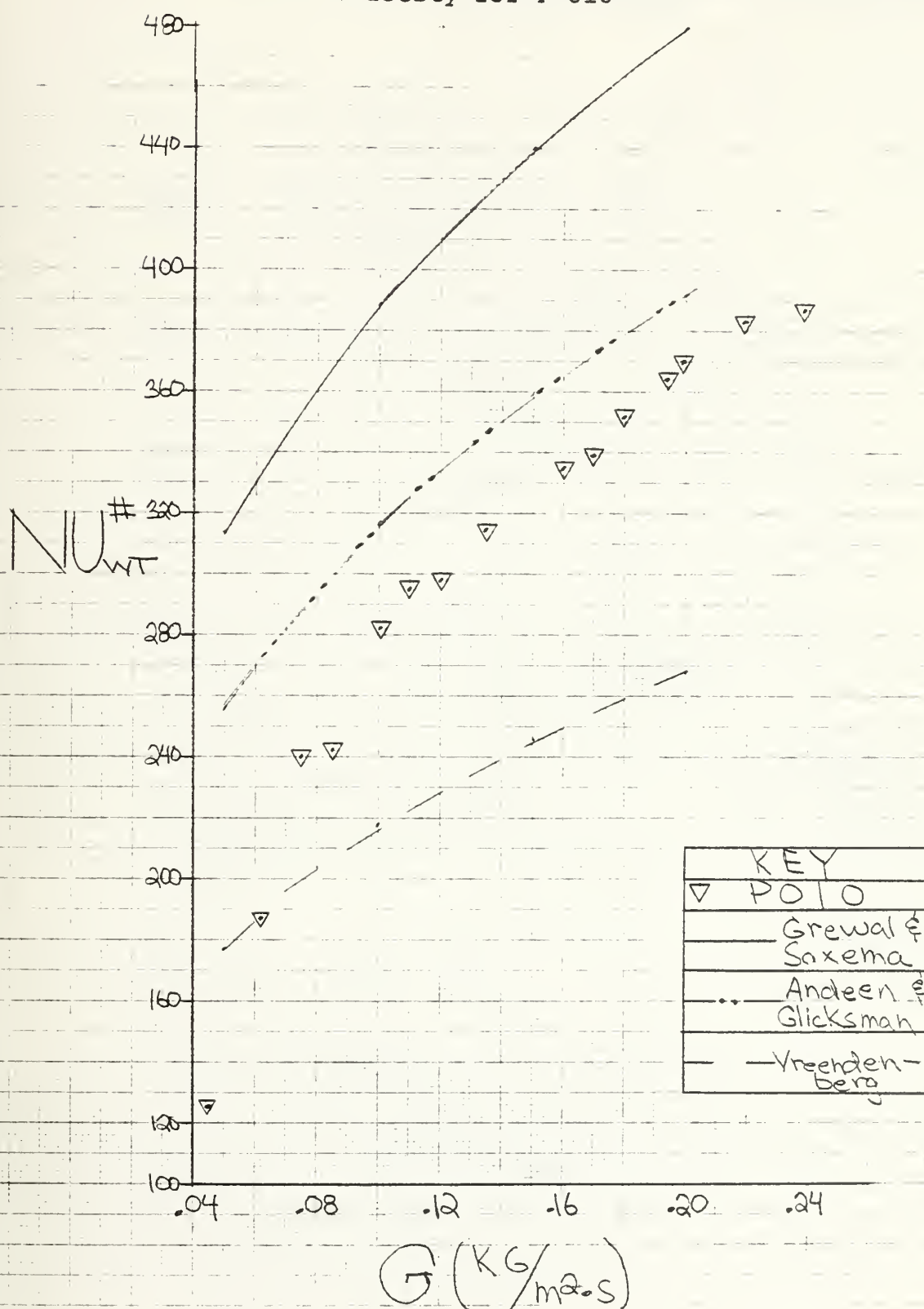


FIGURE 14: Comparison of Experimental to Empirical Nusselt Numbers Against Absolute Mass Velocity for P-023

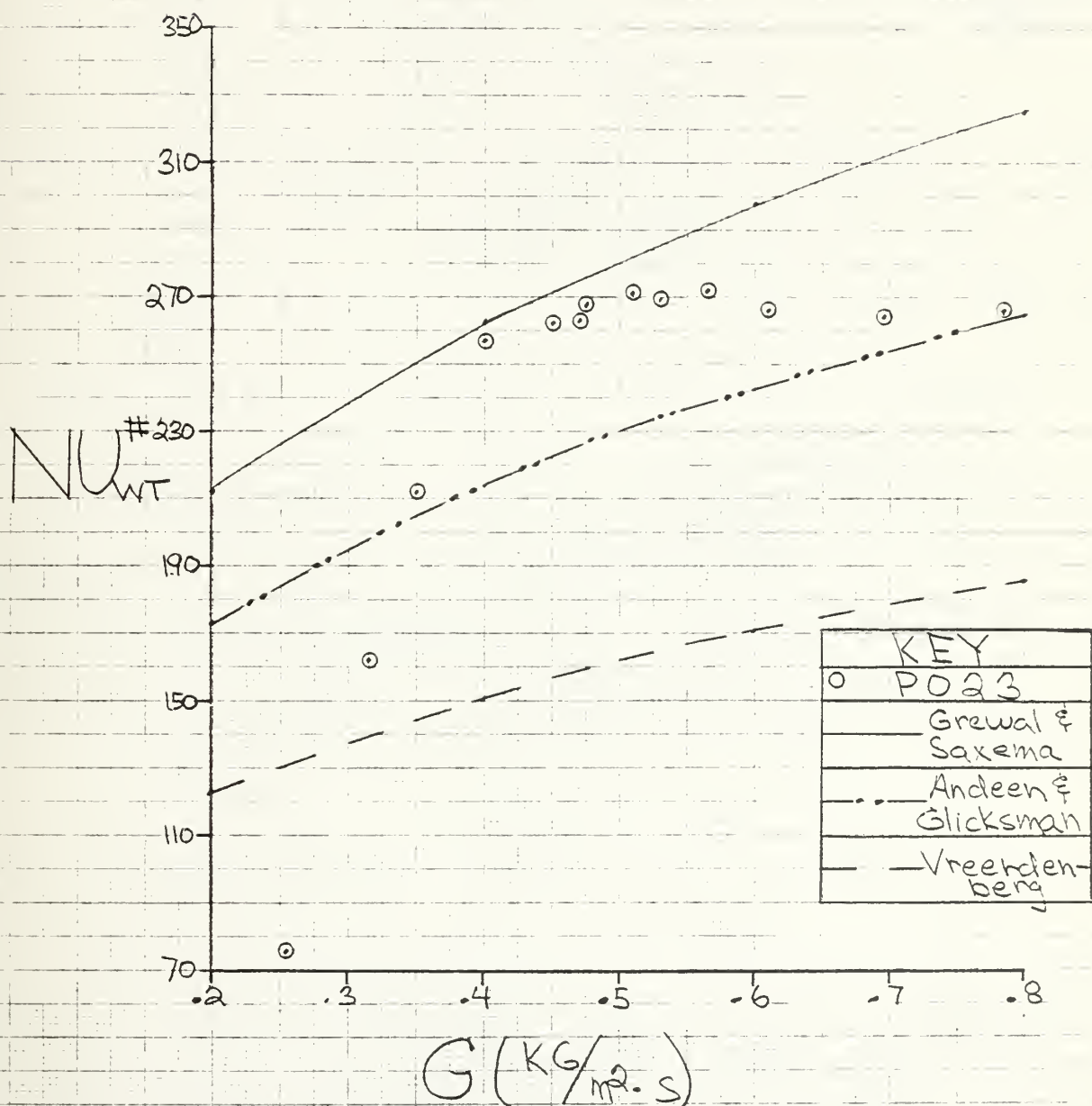


FIGURE 15: Comparison of Experimental to Empirical Nusselt Numbers Against Absolute Mass Velocity for P-047

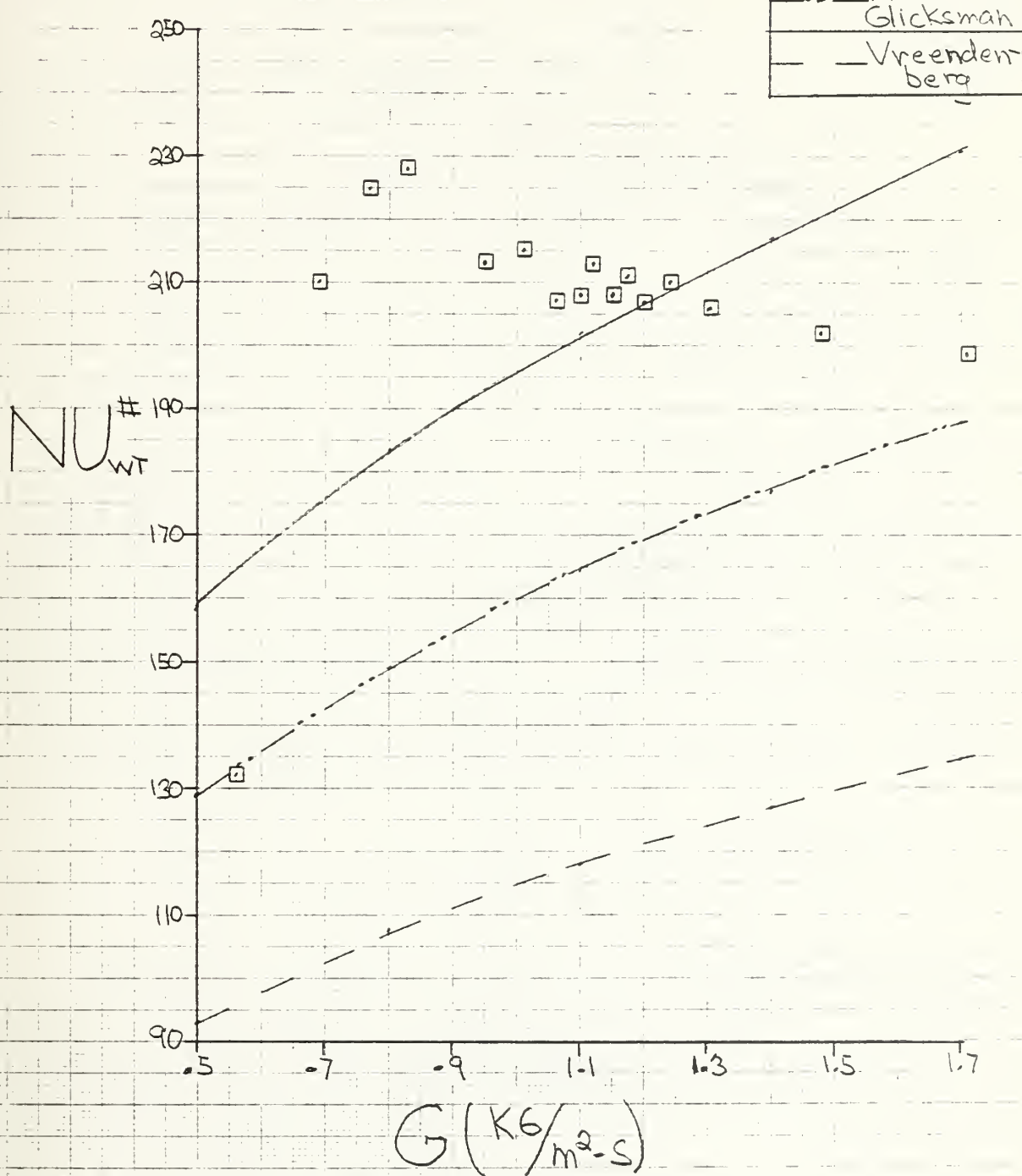


FIGURE 16: Comparison of Experimental to Emperical
Nusselt Numbers Against Absolute
Mass Velocity for A-205

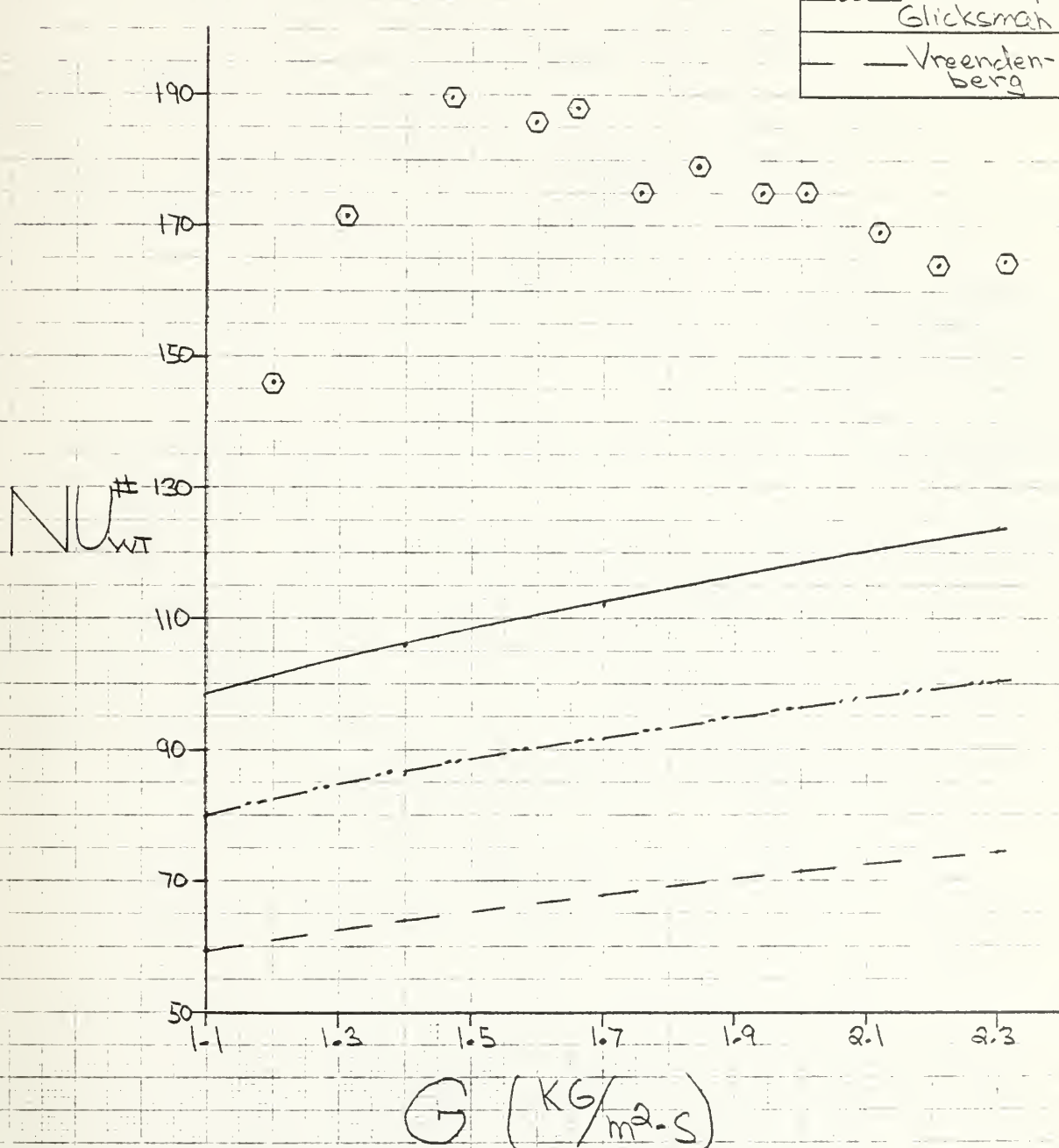
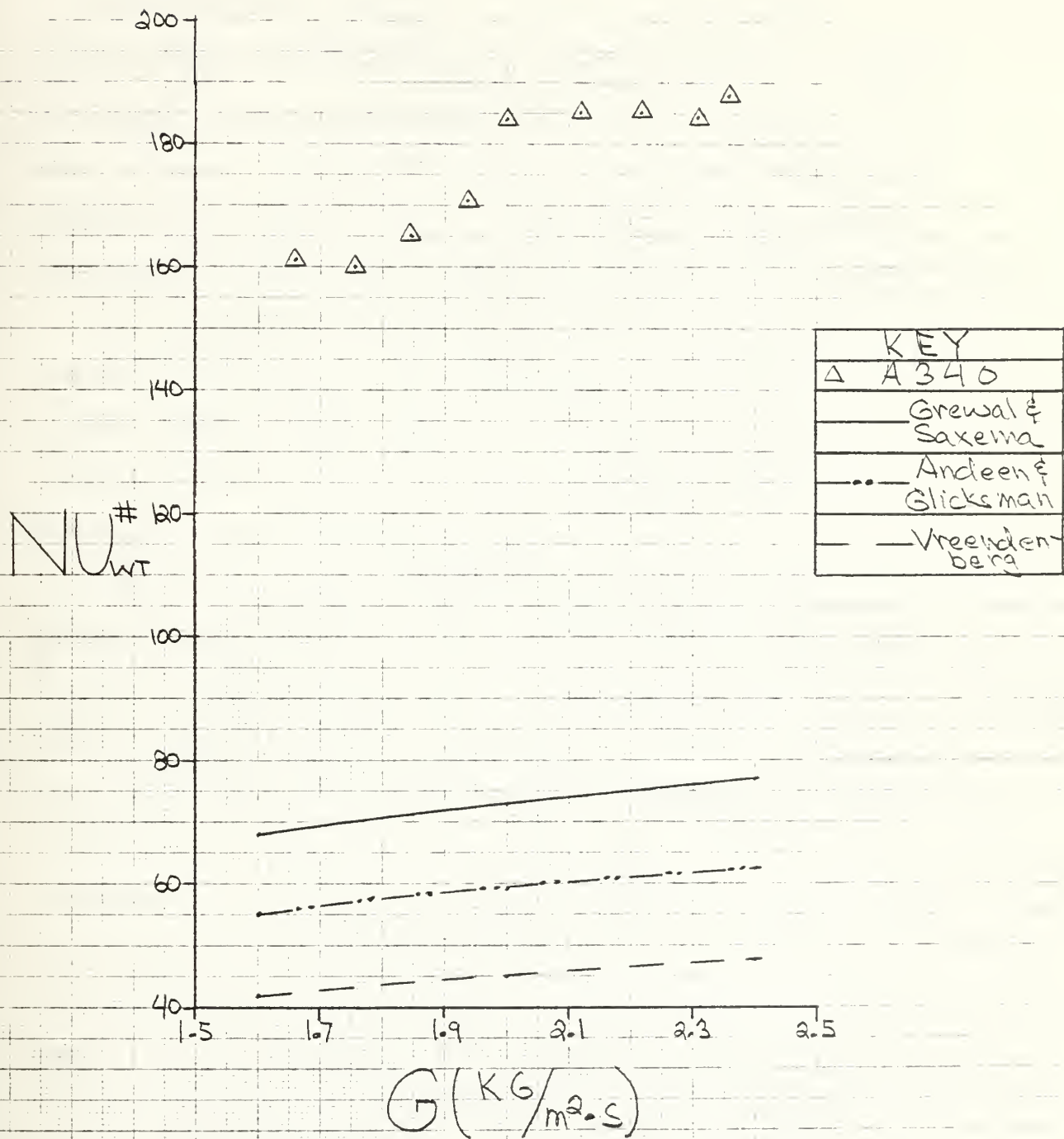


FIGURE 17: Comparison of Experimental to Emperical Nusselt Numbers Against Absolute Mass Velocity for A-340



CONCLUDING REMARKS

Experiments were conducted to identify the heat transfer characteristics particular to the fluidized bed studied. The goal was to quantify the total heat transfer coefficient as a function of the mass velocity for five different fluidized particles. The particles ranged in size from 2.15×10^{-4} m to 3.40×10^{-3} m. Examination of tabulated and graphical data revealed the following generalizations.

The smallest particle sizes tend to have the highest total heat transfer coefficient. So, as bead size increases, the overall heat transfer decreases. The decrease of total heat transfer with increasing particle size is attributed to the successively growing importance of gas convection.

Each particle size exhibited a similar h versus G pattern. The pattern is characterized by a rapid increase in h for a small change in G until a maximum h is achieved at a specific G ; followed by a slowly diminishing h value over all remaining G values. The patterns first stage clearly demonstrates a stronger dependency of h on G for smaller fluidized bead sizes. The superficial velocity which corresponds to the maximum heat transfer coefficient in each case is the optimum velocity for that particle size. This optimum velocity, U_{opt} was experimentally identified for each bead size. Knowing this ideal point will aid subsequent heat transfer experimentation using the same apparatus. The experimentally determined U_{opt} values compare favorably to empirically defined values found from the Todes correlation [11]. The last section of the pattern shows h slowly tailing off. The gradual decrease is caused by the increasing bed

porosity at higher velocities. The larger fluid quantities decrease particle heat conduction, thereby enabling gas convection to dominate the heat transfer process.

The dimensionless Nusselt number was used as a basis for analysis. The Nusselt number based on particle diameter, $NU_p\#$, shows that each bead size has a narrow range of $NU_p\#$ values with the values increasing with particle size. The Nusselt number based on tube wall diameter, $NU_{wt}\#$, was used to directly compare the heat transfer data at all velocities among the various particle sizes. $NU_{wt}\#$ behaved in a manner identical to the behavior of h . The validity of the $NU_{wt}\#$ values was tested against results obtained from numerical correlations by Grewal and Saxena, Andeen and Glicksman, and Vreendenberg. The correlations substantiated findings for the smallest three particles. For the largest two particles, the correlations do not reflect the effects of the large beads. This makes them invalid and were not applied in the analysis.

REFERENCES

1. Botterill, J.S.M., Fluid-Bed Heat Transfer, Academic Press, New York, 1975.
2. Vreedenberg, H.A., "Heat Transfer Between a Fluidized Bed and a Horizontal Tube," Chemical Engineering Science, Vol. 9, 1958, pp. 52-60.
3. Chen, J.C., "Heat Transfer to Tubes in Fluidized Beds," ASME Paper 76-HT-75, ASME-AIChE Heat Transfer Conference, St. Louis, MO., 1976.
4. Andeen, B.R. and Glicksman, L.R., "Heat Transfer to Horizontal Tubes in Shallow Fluidized Beds," ASME Paper No. 76-HT-67, ASME-AIChE Heat Transfer Conference, St. Louis, MO., 1976.
5. Krause, W.B. and Peters, A.R., "Heat Transfer Mechanisms Near Horizontal Heat Exchange Tubes in an Air Fluidized Bed of Uniformly Sized Glass Particles," ASME Paper No. 79-HT-88, ASME-AIChE National Heat Transfer Conference, San Diego, CA., 1979.
6. Grewal, N.S. and Saxena, S.C., "Effect of Surface Roughness on Heat Transfer from Horizontal Immersed Tubes in a Fluidized Bed," ASME Journal of Heat Transfer, Vol. 101, 1979, pp. 297-405.
7. Grewal, N.S. and Saxena, S.C., "Heat Transfer Between a Horizontal Tubes and a Gas-Solid Fluidized Bed," International Journal of Heat and Mass Transfer, Vol. 23, 1980, pp. 1505-1519.
8. George, S.E. and Grace, J.R., "Heat Transfer to Horizontal Tubes in a Pilot-Scale Fluidized Bed," Preprint, ASME-AIChE 20th National Heat Transfer Conference, Milwaukee, WI., 1981.
9. Wade, M.L., M.S. Paper, "Contribution of Gas Convection to Heat Transfer between a Submerged Horizontal Tube and a Fluidized Bed," Pennsylvania State University, 1984.
10. Goroshko, V.D., Rozenbaum, R.B., and Todes, O.M., *Izv. Vysshikh Ucheban. Za vedenii, Nef 4; Gas (Baku) No. 1*, 125, 1958.
11. Toades, O.M., In "Applications of Fluidized Beds in the Chemical Industry," Part II, pp. 4-27, *Izd. "Znanie," Leningrad*.

Thesis

207087

T2764 Terpolilli

Overall heat transfer
coefficients for a hori-
zontal cylinder in a
fluidized bed.

Thesis

207087

T2764 Terpolilli

Overall heat transfer
coefficients for a hori-
zontal cylinder in a
fluidized bed.

thesT2764

Overall heat transfer coefficients for a



3 2768 002 03446 4

DUDLEY KNOX LIBRARY